[illegible]
[illegible]
[illegible] 12
[illegible] 3128
598.

BRIDGMAN CRYSTAL GROWTH

Final Report
Grant NAG-1-397/JFR
Frederick Carlson
Clarkson University
Potsdam, New York 13676

Prepared for

National Aeronautics and Space Administration
Langley Research Center
Hampton, Virginia 23665

January 1990

Contents

1.0 Introduction

The objective of this theoretical research effort was to improve our understanding of the growth of $Pb_xSn_{1-x}Te$ and especially how crystal quality could be improved utilizing the microgravity environment of space. All theoretical growths are done using the vertical Bridgman method. It is believed that improved single crystal yields can be achieved by systematically identifying and studying system parameters both theoretically and experimentally.

A computational model was developed to study and eventually optimize the growth process. The model is primarily concerned with the prediction of the thermal field, although mass transfer in the melt and the state of stress in the crystal were of considerable interest. Ideally these predictions would be combined into a unified package and experimentally verified. This has only partially been done.

This report will present the evolution of the computer simulation and some of the important results obtained. Diffusion controlled growth was first studied since it represented a relatively simple, but nonetheless realistic situation. In fact, results from this analysis encouraged us to study in detail the triple junction region where the melt, crystal, and ampoule wall meet. Since microgravity applications were sought because of the low level of fluid movement, the effect of gravitational field strength on the thermal and concentration field was also of interest. A study of the strength of coriolis acceleration on the growth process during space flight was deemed necessary since it would surely produce asymmetries in the flow field if strong enough. Finally, thermosolutal convection in a steady microgravity field for thermally stable conditions and both stable and unstable solutal conditions was simulated.

2.0 Governing Conservation Equations

The governing equations [cf. 1] for the vertical Bridgman growth system are presented in the following general form:

$$[\frac{\partial}{\partial t}(\Gamma \phi) + \nabla \cdot (\Gamma \phi U)] + \frac{\partial \varphi}{\partial t} + \nabla \cdot (\phi U) = \nabla \cdot (\frac{\delta}{\rho_o} \nabla \phi) + \frac{\sigma}{\rho_o}$$

where

$$\rho = \rho_o + \rho'(x,t) \ = \text{density},$$

$$\Gamma = \rho'/\rho_o,$$

and

Variable	Mass	Energy	Species	r-Momentum	z-Momentum
ϕ	1	$C_p T$	C	u	w
δ	0	K/C_p	D	μ	μ
σ	0	0	0	$-\frac{\partial p}{\partial r}$	$-\frac{\partial p}{\partial z} + \rho g_z$

State: Equilibrium phase diagram

The interfacial conditions are:

Species continuity: $D \frac{\partial c}{\partial n} = V_f (k - 1) C$

Energy:
$$\left(K \frac{\partial T}{\partial n}\right)_s - \left(K \frac{\partial T}{\partial n}\right)_l = \rho H A \frac{\partial f}{\partial t}$$

Side conditions:

Furnace walls - Either temperature specified or adiabatic (in the region between the hot and cold zones.

Furnace-Ampoule Gap - Either radiation dominated or a heat transfer coefficient is specified.

Melt - No slip condition at ampoule walls.

This is the exact form of the equations and is the starting point in our computer codes. The term in the brackets, [ ], is set equal to zero if the Boussinesq approximation is invoked. The model based on this set of equations and side conditions was solved by a finite element method and a technique similar to the classical Marker and Cell [2-6].

3.0 Diffusion Controlled Heat and Mass transfer

The limiting case of advectionless heat and mass transfer was completed in order to gain some insight into the problem. It is relatively easy to solve this case in which only the energy and species transport equations are important. The geometry and operating conditions are shown in Figure 3.1. These conditions are similar to an experiment which was conducted at Langley Research Center. A large aspect ratio charge with an extended quartz ampoule region at each end is initially placed in the furnace with the bottom of the ampoule in the center of the adiabatic zone. The charge is completely melted and homogeneous at this point in time. The zero strength gravity field present will result in no fluid motion throughout the process.

The furnace Biot number is chosen to be very large making the outside of the ampoule the same temperature as the adjacent furnace zone. The top and bottom of the ampoule are also held at the hot and cold zone temperatures, respectively. Figure 3.2 shows the interface position as a function of time. A position of zero corresponds to the bottom of the charge which is 5 cm above the bottom of the ampoule. The melt first starts to solidify near the ampoule wall. At 10,077 s from the start of the process 90% of the bottom of the the ampoule is still in contact with the melt. Solidification proceeds in an axisymmetric manner and is characterized by significant radial diffusion until another 2,000 s have elapsed and steady state conditions prevail. At all times the interface is concave.

Figure 3.3 shows axial concentration profiles at various distances from the center of the ampoule. Two different ampoule pull rates are given, but the qualitative picture is the same. Steady state conditions prevail after about 1.5 cm of growth. Prior to this large radial segregation is present as the transient concentration field and interface velocity adjust (Figure 3.4).

Slower growth rates produce more segregation. This can clearly be seen in Figure 3.5 where the steady state concentration profiles are compared for two different growth rates. The transient profile at axial position 5.2 cm is characterized by a maximum at a dimensionless radius of 0.8. The first to solidify is nearest the wall. Mass transfer then proceeds both radially and axially in this region. As the solidified region in the transient state approaches the centerline of the ampoule the relatively flat interface produces little radial segregation over the middle 80% of the charge. This is in contrast to the steady state segregation profile beyond the 7.0 cm axial position. This nonuniform concentration profile is due to the highly concave interface which is solely due to the thermal field. Adjustment of the thermal field could lead to a radically different interface shape and segregation pattern.

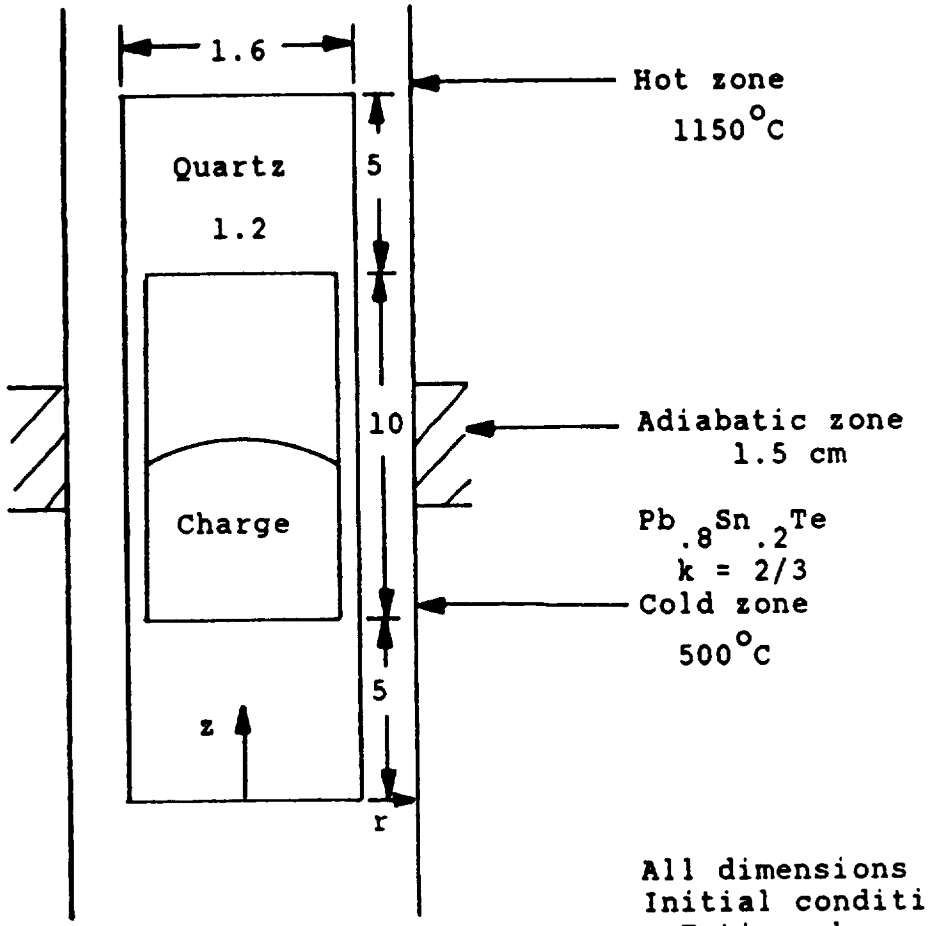

All dimensions in cm
Initial condition:
Entire charge liquid and homogeneous. Bottom of ampoule centered in the adiabatic zone. Hot and cold zone Biot numbers are infinite.

Figure 3.1 Diffusion controlled extended ampoule simulation.

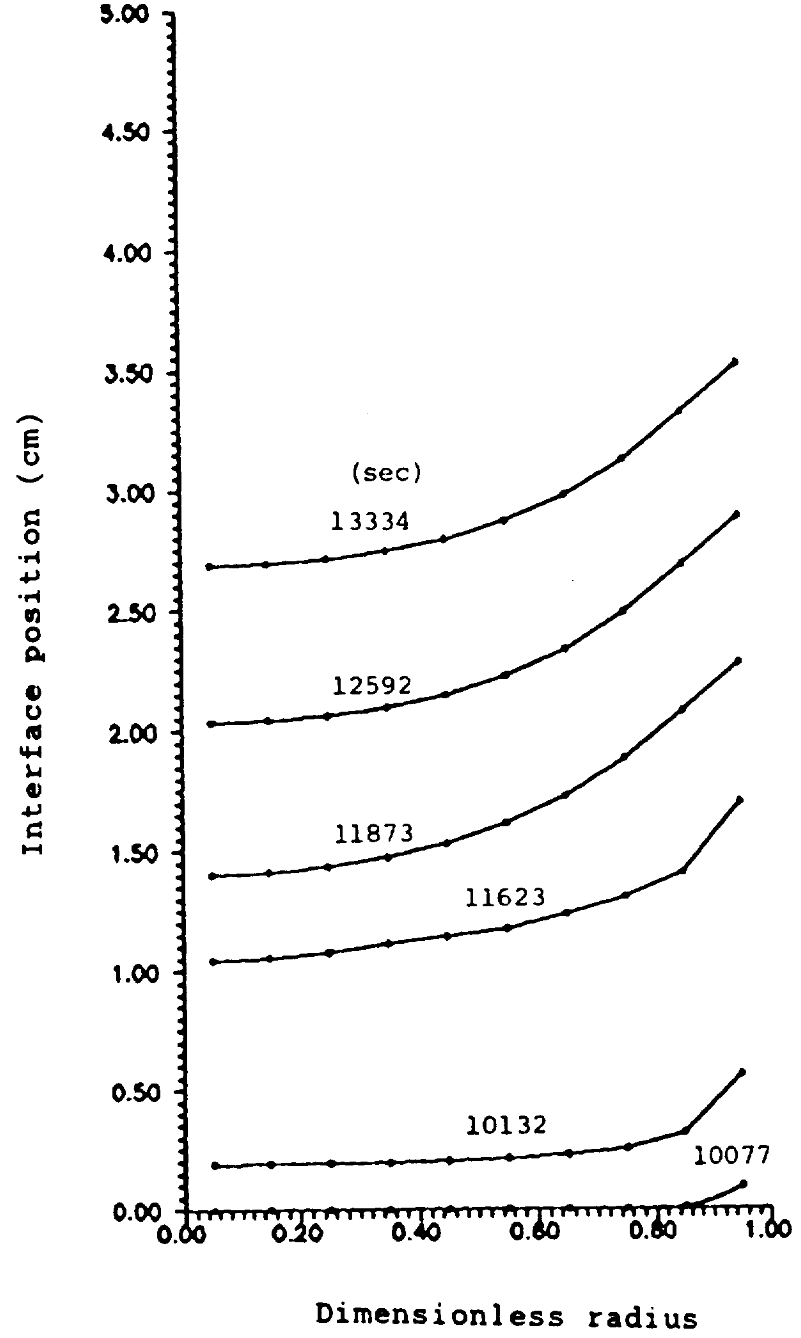

Figure 3.2 Interface morphology at an ampoule pulling rate of 1.5 cm/hr and segregation coefficient of 2/3.

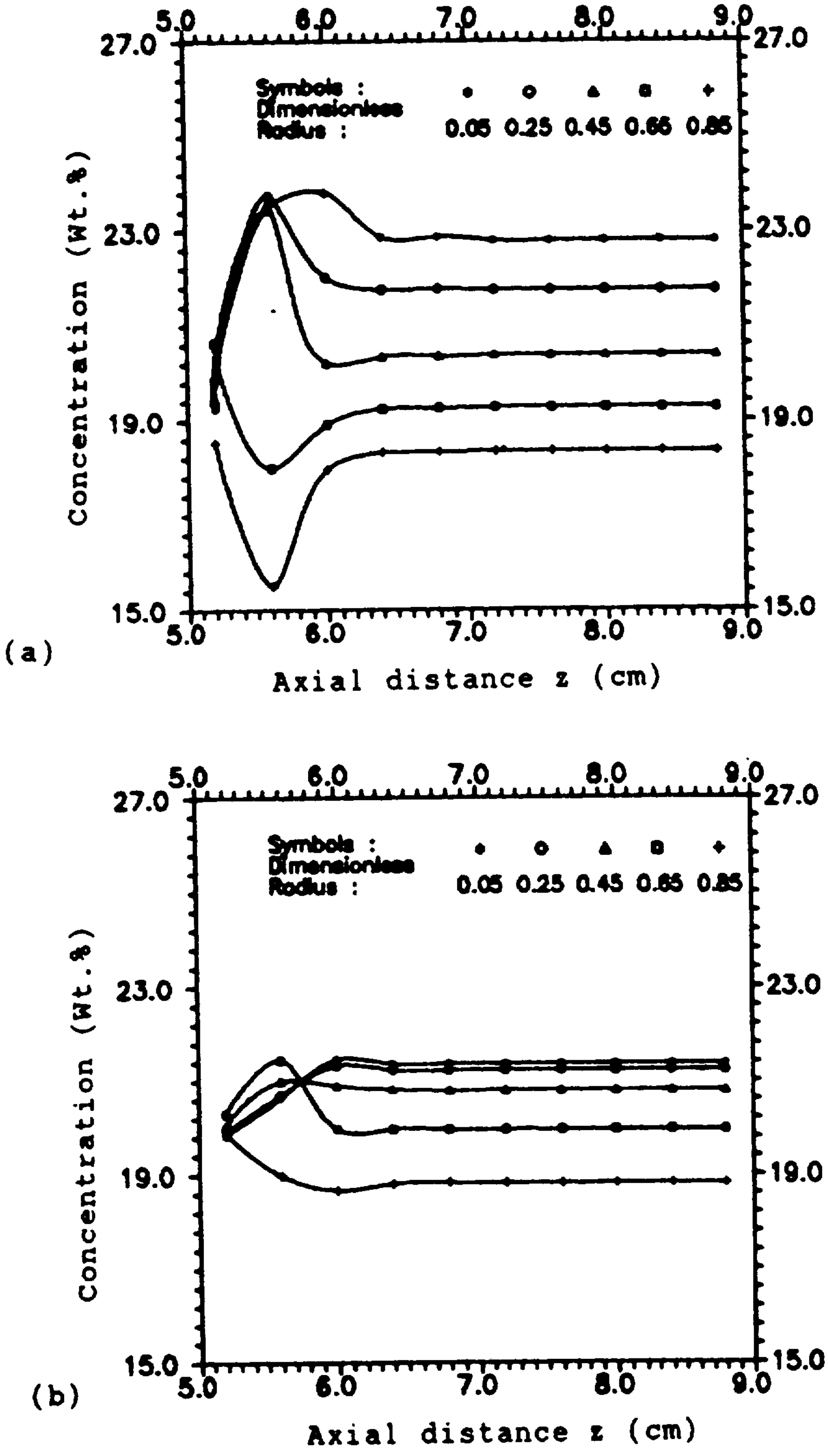

Figure 3.3 Concentration versus axial distance for (a), V_{pull}=0.35 cm/hr and (b), V_{pull}=1.50 cm/hr.

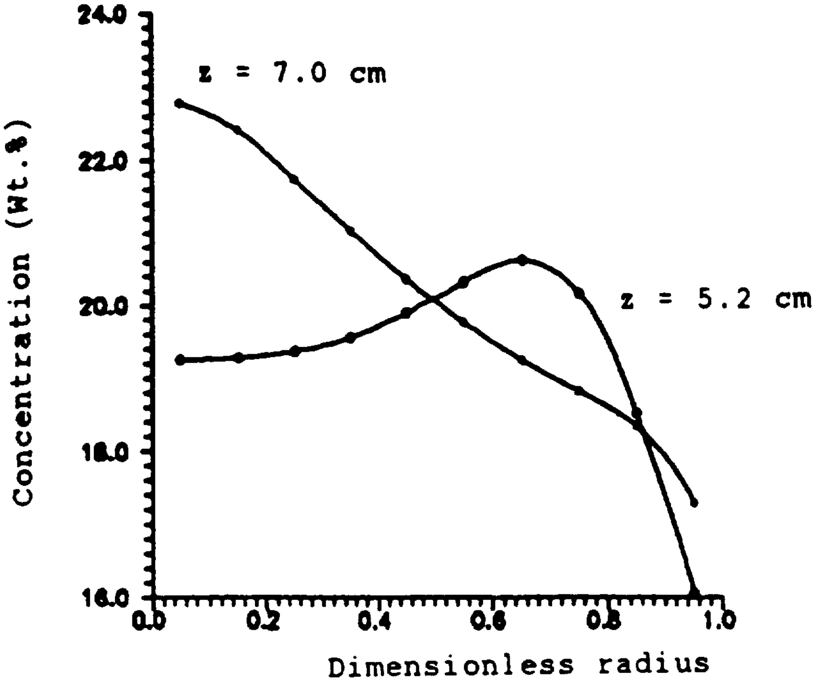

Figure 3.4 Concentration versus dimensionless radius when V_{pull}=0.35 cm/hr and (a), transient conditions, z = 5.2 cm and (b), steady state conditions, z = 7.0 cm.

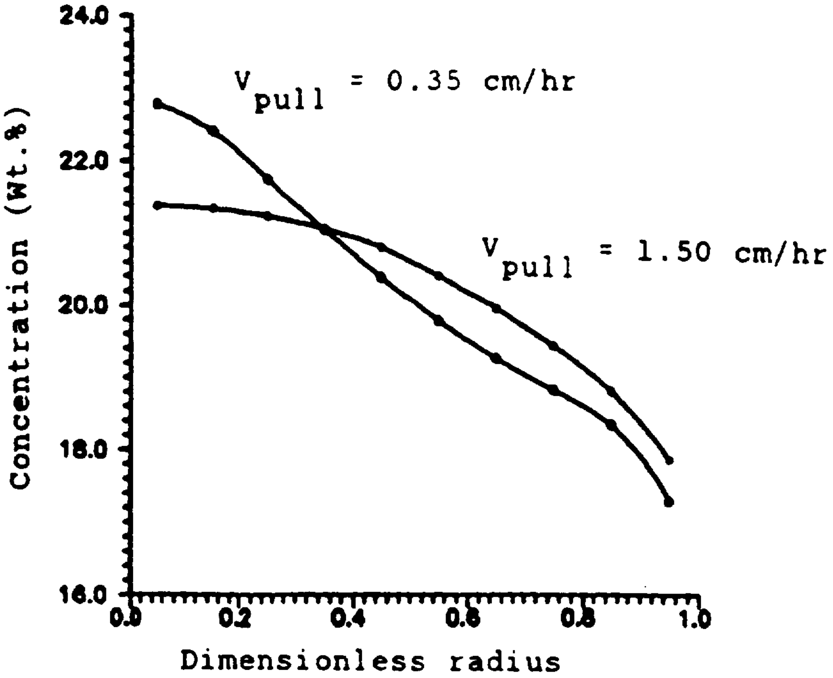

Figure 3.5 Steady state concentration versus dimensionless radius for different pull rates.

4.0 Triple-Junction

Furnace hot and cold zone temperature profiles and adiabatic zone thickness strongly influence the shape and position of an interface[7]. Interface shape in turn strongly controls segregation. This has been shown in diffusion dominated growth[8,9]. These studies were conducted without considering the effect of the ampoule on the process. The ampoule has a major influence on the heat transfer between the hot and cold zones, and it also effects the interface. This was determined by our model for the case of conduction dominated heat transfer. This approximate case is very close to the real situation for low Prandtl number melts as long as the fluid velocity in the vicinity of the interface is not too large.

In order to study the effect of the ampoule, charge, and pull rate on the interface the system shown in Figure 4.1 was used as a representative example. An ampoule with 0.2 cm thick walls contains a 2.0 cm diameter charge. The outside walls of the ampoule are insulated, a condition which simulates an ampoule in an adiabatic zone. The length of the charge - ampoule - adiabatic zone is 4.0 cm and it is bounded on the top and bottom planes by isotherms such that the system experiences an axial gradient of 50^{o}K/cm. These planes do not have to be isotherms, and their temperature distribution can be easily adjusted to other values based on actual furnace hot and cold zone conditions[7]. The interface temperature is chosen to be the average of the hot and cold zone axial isotherms. If all diffusivities are equal and the ampoule is stationary, the interface will be located at position z = 2.0 cm. The range of thermophysical properties used are representative of quartz or pyrolytic boron nitride ampoules and charges of lead tin telluride or mercury cadmium telluride. The interface is characterized by its centerline position in the zone, (z_o), and its curvature index, ((z_o-z_w)/a). Calculations for twenty one cases were made and are presented in Table 4.1. The influence of pull velocity, latent heat, and thermal diffusivity ratios are summarized below.

Pull Velocity - V_p

Ampoule withdrawal velocity influences the heat transfer within the governing conservation equation and through the interfacial boundary condition.

A. Cases: 1,2

Constant: Latent heat, a_w/a_s, a_l/a_s = 0, 1.0, 1.0

V_p(m/s)	(z_o-z_w)/a	f position (cm)
0.0	0.0	2.000
$-1.0(10^{-5})$	0.0	1.931

Moving the ampoule with no latent heat release and uniform properties simply lowers the interface isotherm. Planar interfaces remain planar.

B. Cases: 16,20

Constant: Latent heat, a_w/a_s, a_l/a_s = 180.0, 2.5, 2.0

V_p(m/s)	(z_o-z_w)/a	f position (cm)
$-1.0(10^{-5})$	-0.099	1.149
$-2.0(10^{-5})$	-0.123	0.914

With $a_l/a_s > 1$, the interface is concave when the pull velocity is zero. Moving the ampoule not only lowers the interface but makes it more concave.

C. Cases: 17,21

Constant: Latent heat, a_w/a_s, a_l/a_s = 180.0, 1.25, 0.5

V_p(m/s)	$(z_o-z_w)/a$	f position (cm)
$-1.0(10^{-5})$	0.039	2.325
$-2.0(10^{-5})$	0.021	2.122

With $a_l/a_s < 1$, the interface is convex when the pull velocity is zero. Moving the ampoule lowers the interface and makes it less convex. At a certain pull rate it might be possible to approach a planar interface.

Latent Heat (cal/g)

Latent heat influences the heat transfer only through the interfacial boundary condition where it combines with the pull velocity.

D. Cases: 2,3,15

Constant: V_p, a_w/a_s, a_l/a_s = $-1.0(10^{-5})$ m/s, 1.0, 1.0.

Latent Heat	$(z_o-z_w)/a$	f position (cm)
0.0	0.0	1.931
36.0	-0.003	1.894
360.0	-0.037	1.484

When all diffusivities are equal, a zero latent heat allows the pull velocity to translate the planar interface downward. As the magnitude of latent heat increases, more energy is released at the interface which moves closer to the cold zone. The solid melts less in the vicinity of the ampoule because some of this energy release passes through the ampoule wall instead of melting solid and lowering the interface as it does at the center of the charge.

E. Cases: 14,16,18

Constant: V_p, a_w/a_s, a_l/a_s = $-1.0(10^{-5})$ m/s, 2.5, 2.0.

Latent Heat	$(z_o-z_w)/a$	f position (cm)
0.0	-0.053	1.417
180.0	-0.099	1.149
360.0	-0.111	0.976

As either a_l/a_s increases from 1 or latent heat increases the interface becomes concave. These effects are additive making the interface more concave.

F. Cases: 11,17,19

Constant: V_p, a_w/a_s, a_l/a_s = $-1.0(10^{-5})$ m/s, 1.25, 0.5

Latent Heat	$(z_o-z_w)/a$	f position (cm)
0.0	0.062	2.481
180.0	0.039	2.325
360.0	0.027	2.177

As a_l/a_s decreases from 1 or latent heat increases the interface becomes convex or concave, respectively. These competing effects are additive and conceivably could be tuned to provide any interface desired.

Diffusivity Ratio a_l/a_s

G. Cases: 2,4-14

Constant: Latent heat, V_p, a_w/a_s = 0.0, $-1.0(10^{-5})$m/s, various values between 0.5 and 2.5.

a_l/a_s	$(z_o-z_w)/a$	f position (cm)	Cases
< 1	convex	above 1.931	9,10,11
= 1	planar	1.931	2,5,6
> 1	concave	below 1.931	4,7,8,& 12,13,14

Diffusivity Ratio a_w/a_s

As the following examples illustrate, for increasing a_w/a_s,

i. the interface moves toward the center(z = 2.0),

ii. concave interfaces become more concave, and

iii. convex interfaces become more convex.

H. Cases: 4,7,8

Constant: Latent heat, V_p, a_l/a_s= 0.0, $-1.0(10^{-5})$m/s, 10.0

a_w/a_s	$(z_o-z_w)/a$	f position (cm)
0.5	-0.012	0.398
1.0	-0.021	0.417
2.0	-0.099	0.439

I. Cases: 12,13,14

Constant: Latent heat, V_p, a_l/a_s= 0.0, $-1.0(10^{-5})$m/s, 2.0

a_w/a_s	$(z_o-z_w)/a$	f position (cm)
0.5	-0.014	1.308
1.5	-0.041	1.369
2.5	-0.053	1.417

J. Cases: 2,5,6

Constant: Latent heat, V_p, a_l/a_s = 0.0, $-1.0(10^{-5})$m/s, 1.0

Diffusivity ratio a_w/a_s has no effect on either the interface shape or position.

K. Cases: 9,10,11

Constant: Latent heat, V_p, a_l/a_s = 0.0, $-1.0(10^{-5})$m/s, 0.5

a_w/a_s	$(z_o-z_w)/a$	f position (cm)
0.25	0.015	2.564
0.75	0.035	2.513
1.25	0.062	2.481

These experiments highlight the effect of the ampoule on interface shape. It is the thermal resistance of the wall which is of importance. A thicker wall will offer less resistance and distort the interface over a larger radius than a thin wall of the same material.

Case	H (cal/g)	$V_p(-1*10^{-5})$ (m/s)	a_w/a_s	a_l/a_s	$(z_o-z_w)/a$	Position (cm)
1	0.0	0	1.0	1.0	0.000	2.000
2	0.0	1	1.0	1.0	0.000	1.931
3	36.0	1	1.0	1.0	-0.003	1.894
4	0.0	1	1.0	10.0	-0.021	0.417
5	0.0	1	0.5	1.0	0.000	1.931
6	0.0	1	2.0	1.0	0.000	1.931
7	0.0	1	0.5	10.0	-0.012	0.398
8	0.0	1	2.0	10.0	-0.099	0.439
9	0.0	1	0.25	0.5	0.015	2.564
10	0.0	1	0.75	0.5	0.035	2.513
11	0.0	1	1.25	0.5	0.062	2.481
12	0.0	1	0.5	2.0	-0.014	1.308
13	0.0	1	1.5	2.0	-0.041	1.369
14	0.0	1	2.5	2.0	-0.053	1.417
15	360.0	1	1.0	1.0	-0.037	1.484
16	180.0	1	2.5	2.0	-0.099	1.149
17	180.0	1	1.25	0.5	0.039	2.325
18	360.0	1	2.5	2.0	-0.111	0.976
19	360.0	1	1.25	0.5	0.027	2.177
20	180.0	2	2.5	2.0	-0.123	0.914
21	180.0	2	1.25	0.5	0.021	2.122

Table 4.1 Triple Junction Numerical Experiment

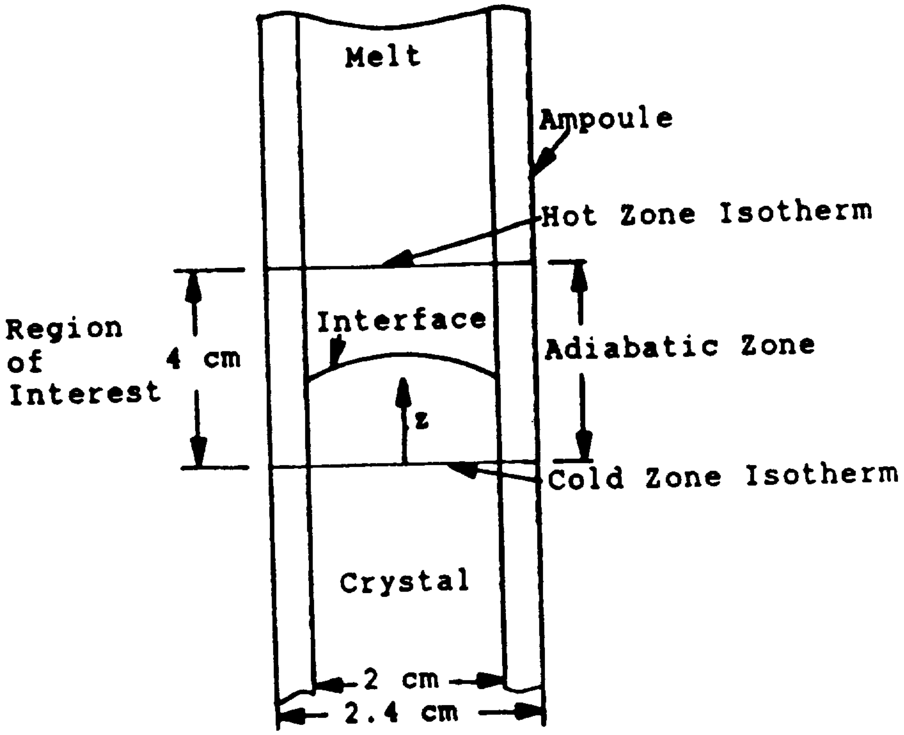

Diffusion controlled heat transfer

Axial gradient ($^oK/cm$): 50.0
Latent heat (cal/g): 0 to 360.
a_w/a_s: 0.25 to 2.5
a_l/a_s: 0.5 to 10.

Figure 4.1 Triple Junction geometry, thermophysical properties, and boundary conditions.

5.0 Effect of Gravitational Field Strength on Steady Thermal Convection

It is well known that melt advection exerts a strong influence on the processes that control the growth of compound semiconductor crystals. In Bridgman crystal growth advection is driven by density differences in the melt interacting with the local gravitational field. Many of the problems encountered when trying to produce homogeneous, defect free crystals, are attributed directly to melt advection through its influence on the heat and mass transport during solidification. Consequently, measures are usually taken to minimize advection and to enhance growth in the diffusively dominant regime which is better understood and thus easier to control. The microgravity environment of space offers a technique and provides an excellent laboratory to study gravitationally induced advection.

Crystals grown in space are usually quite different from their earth based counterparts grown under otherwise similar conditions. These differences cannot be explained using the currently available mathematical models with analytical solutions (e.g.,[10,11]), because their inherent simplifying assumptions usually tend to discard some important details of the physical phenomena which control crystal growth. Order of magnitude studies (e.g.,[12]) have also yielded useful information, but again, are lacking in the fine detail necessary to explain the different results of experiments. Relatively simple analytic or computational models which only consider diffusion (e.g.,[8]) are also inadequate in studies concerned with trying to understand the physics of crystal growth since advection strongly influences the solidification process.

The objective of this section is to more completely understand the role of melt advection in the transport process. Advection has not been universally established to be detrimental in all instances. Maybe through a higher level of understanding it will be possible to control the advection and optimize the growth process. The computational model considers many of the important effects, including combined advective and diffusive transport(convection) and body forces induced by density differences in the melt. In order to simplify the calculations this study was done on an axially symmetric, thermally driven flow, in which the gravitational field was aligned with the vertical axis. Only a stationary ampoule without solutal convection was considered. However, the influence of the ampoule wall was included. Gravitational field strength was varied systematically and its effect on the growth process ascertained for typical furnace conditions.

An ampoule, insulated on both its top and bottom, is placed in the middle of a furnace which has a large adiabatic zone (Figure 5.1). The furnace hot and cold zones maintain the ampoule wall at constant temperature levels above and below the charge melting point. The ampoule is made of fused silica, has 0.185 cm thick walls, an outer diameter of 1.905 cm, and an overall length of 7.62 cm. The stationary ampoule contains a charge similar to a Germanium-Silicon compound except that the solutal coefficient of volume expansion has been set equal to zero. Because the charge contracts upon solidification, the top of the melt is not held in contact with the ampoule. This free surface should more closely simulate actual processing conditions. Thermophysical properties of the system are also given in Figure 5.1.

The gravitational field strength was allowed to vary from g_e to $10^{-8} g_e$ in five steps. The velocity and temperature fields resulting from this systematic variation are presented in Figures 5.2-5.6 in which only half of the r-z plane is displayed. The strongest circulation at any gravitational level is always in the largest cell which is adjacent to the wall in the vicinity of the junction between the adiabatic and hot zone. Cell circulation is counterclockwise with the flow upward along the wall, as denoted by the positive value of streamfunction. The center of any cell is the maximum value of streamfunction for that cell. Equal streamfunction increments are then shown between the center of each cell and the zero value on the ampoule wall. Adjacent cells always rotate in opposite directions.

As gravity decreases, both the quantitative and qualitative nature of the flow and transport change. Four cells decrease to one and then increase to two, but the nature of the flow has changed in the process. The horizontally stratified cells of Figure 5.2 give way to the unicellular flow of Figure 5.4 which in turn yields to the vertical cell pattern of Figure 5.6. This could have a substantial influence on the transport process if the transport is advection dominated. Semiconductor melts typically have Prandtl and Schmidt numbers on the order of 0.01 and 100.0, respectively. Consequently, while rather vigorous advection will be necessary to influence heat transport ($G > 10^{-4}$, given below), species transport is altered at much lower melt velocities. This is further discussed in Section 7. If included, the species distribution would be nearly uniform within the cells of Figure 5.2. Species transport between cells however would be primarily by diffusion making the horizontally stratified field considerably different than the vertical field. This horizontal rather than vertical solutal stratification could have a profound effect on the solute segregation in the crystal.

Three conditions govern the interface shape and radial distribution of normal temperature gradient once a given charge and furnace conditions are set. These are zone junction, triple junction, and melt advection. Zone junction occurs because energy enters and leaves the system radially but is mostly axial in regions well within the adiabatic zone. In areas where adiabats are largely radial, an isothermal interface will be highly curved. Long adiabatic zones yield a region of parallel isotherms and promote planar interfaces. Without advection or an ampoule wall, this is the sole condition which determines the interface shape. When the interface is planar and far from the zone junctions, that is, hot-adiabatic or cold-adiabatic junctions, the radial distribution of interface normal temperature gradient is constant. If the length of the adiabatic zone is not long enough to have parallel isotherms, then the interface may be convex, concave, or planar and the normal temperature gradient increases with radius.

Extending the pure conduction case by adding a wall produces an interesting result in the region of the triple junction where the wall, melt, and crystal meet. Differences in thermal conductivity between the three mediums distort the interface. When the heat transfer is conduction dominated, the triple junction effect moves the interface upward when the wall conductivity is greater than that of the crystal (current example). The opposite, a downward shifting of the interface, is true when the wall-crystal conductivity ratio is reversed. The degree of deviation of the interface from the planar form depends on the magnitude of this conductivity ratio. This cannot be seen in Figure 5.7 because of the relatively coarse grid used in the calculation in the triple junction region and the small difference between the conductivities of the wall and crystal. It is the primary reason for the increase in normal temperature gradient near the triple junction given in Figure 5.8 for $G < 10^{-4}$. Including the wall, with $K_l > K_w > K_s$, some thermal energy from the melt, which previously went into the crystal when all conductivities were equal, now goes into the wall resulting in an increase in flux with radius. This triple junction effect is clearly shown in Figure 5.8 when conduction dominates at G levels less than 10^{-4}. Zone junction plays only a minor role because of the rather long adiabatic zone as can be seen from the parallel melt isotherms in the vicinity of the interface.

The third condition, melt advection, is dominant in energy transport at G levels above 10^{-4}. Figure 5.9, a plot of total energy transferred from the hot zone to the cold zone for various gravity strengths, indicates a maximum transport of energy at G = 1 followed by a rapid decline to a constant value at G = 10^{-4}. While not shown, the ratio of advected to conducted energy transport at G levels of 1, 10^{-2}, and 10^{-4} is 17.64%, 5.25%, and 0.0%, respectively. A strong downward movement of the interface is shown in Figure 5.7 as advection becomes more vigorous at higher G levels. With advection present the flux distribution is further modified, starting at a higher level than the pure conduction mode at the ampoule centerline, reaching a maximum, and then decreasing near the wall. The upper circulation cell advects additional energy to the region of the interface at the ampoule centerline. The remaining three cells, in conjunction with the wall, have the net effect of reducing the flux at the wall. The increase and then decrease in the normal temperature gradient as shown in Figure 5.8 is due to the combined effects of triple junction and advection. Again advection no longer alters the gradient at low gravitational levels. It is difficult to generalize what the combined effect melt advection and the triple junction has on constitutional supercooling from such limited data.

Thermal convection phenomenon in Bridgman-Stockbarger experiments, under varying gravitational conditions, was simulated over a wide range of conditions by the computational model. The results of a limited number of calculations indicated that, as expected, if gravitational field strength can be reduced to a level lower than four orders of magnitude below Earth based conditions, then advection effects can be neglected when calculating the thermal transport of low Prandtl number materials. The same of course cannot be said for the species transport.

The current calculations did not consider other possible important effects which exist under reduced gravity conditions. These include (1) coriolis acceleration, (2) surface tension, and (3) accelerations resulting from orbital control requirements.

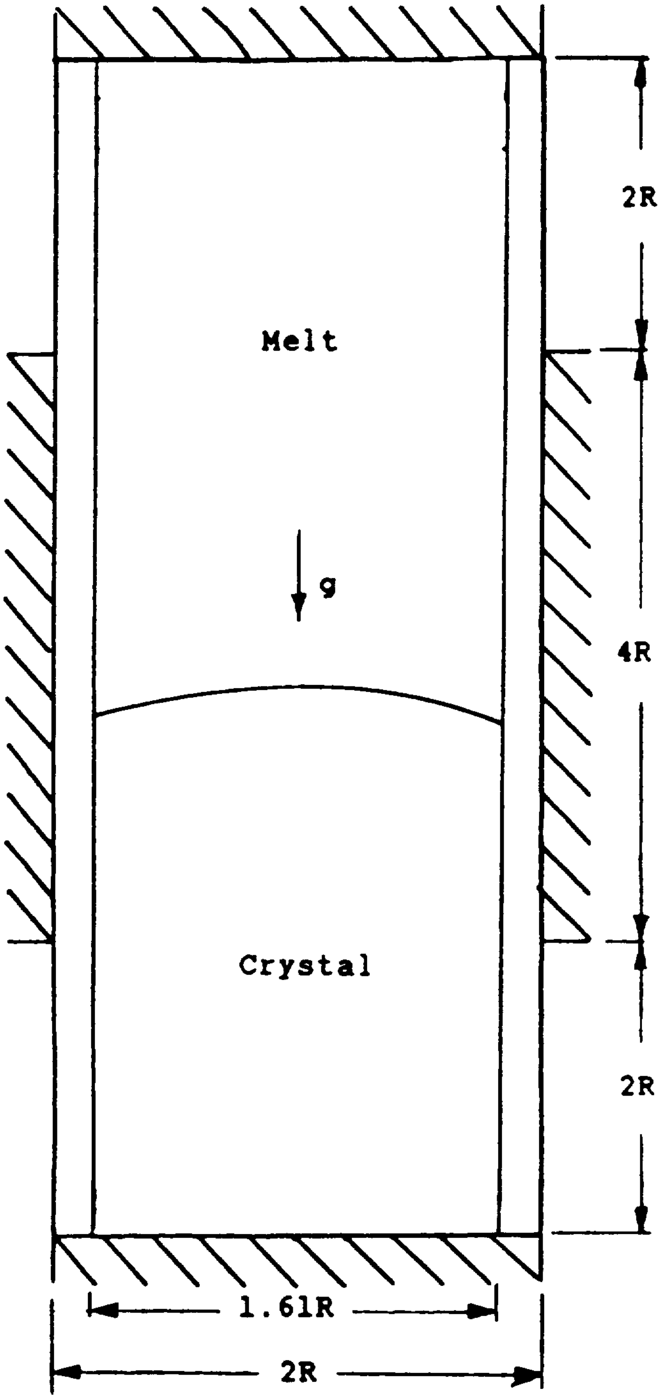

$C_p = 0.39$ cal/g K

$Pr = 5.88(10^{-3})$

$R = 0.9525$ cm

$T_c = 765$ C

$T_f = 937$ C

$T_h = 1070$ C

$\beta_t = 5(10^{-4})$ /K

$a_w = 0.1247$ cm^2/s

$a_l = 0.1870$ cm^2/s

$a_s = 0.0815$ cm^2/s

$\rho = 5.48$ g/cm^3

$\nu = 1.10(10^{-3})$ cm^2/s

Figure 5.1 Geometry and thermophysical properties for thermal convection study.

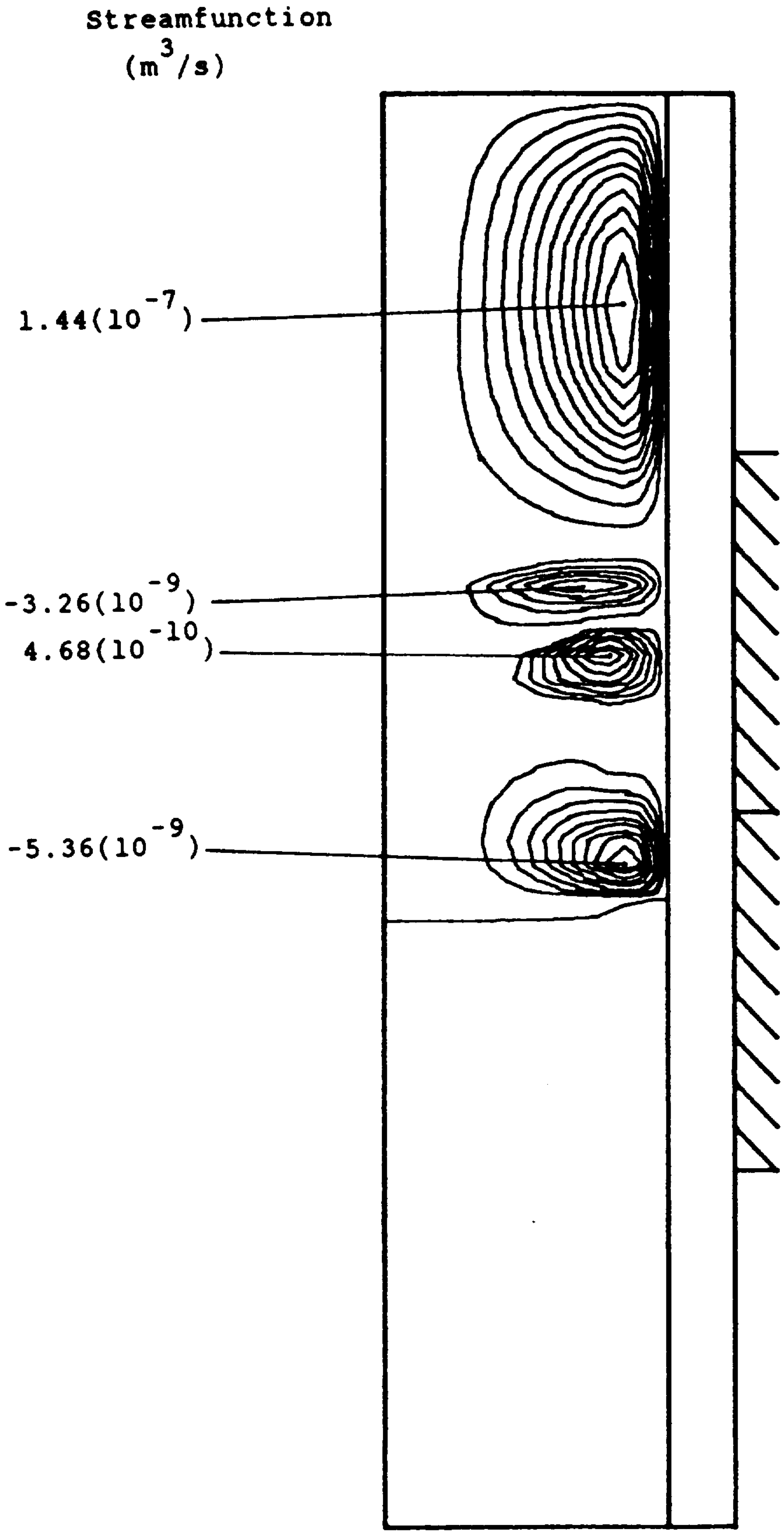

Figure 5.2 Thermal convection streamlines. $V_{max} = 2.7(10^{-2})$ m/s, Gravitational field strength = 9.8 (10^0) m/s^2.

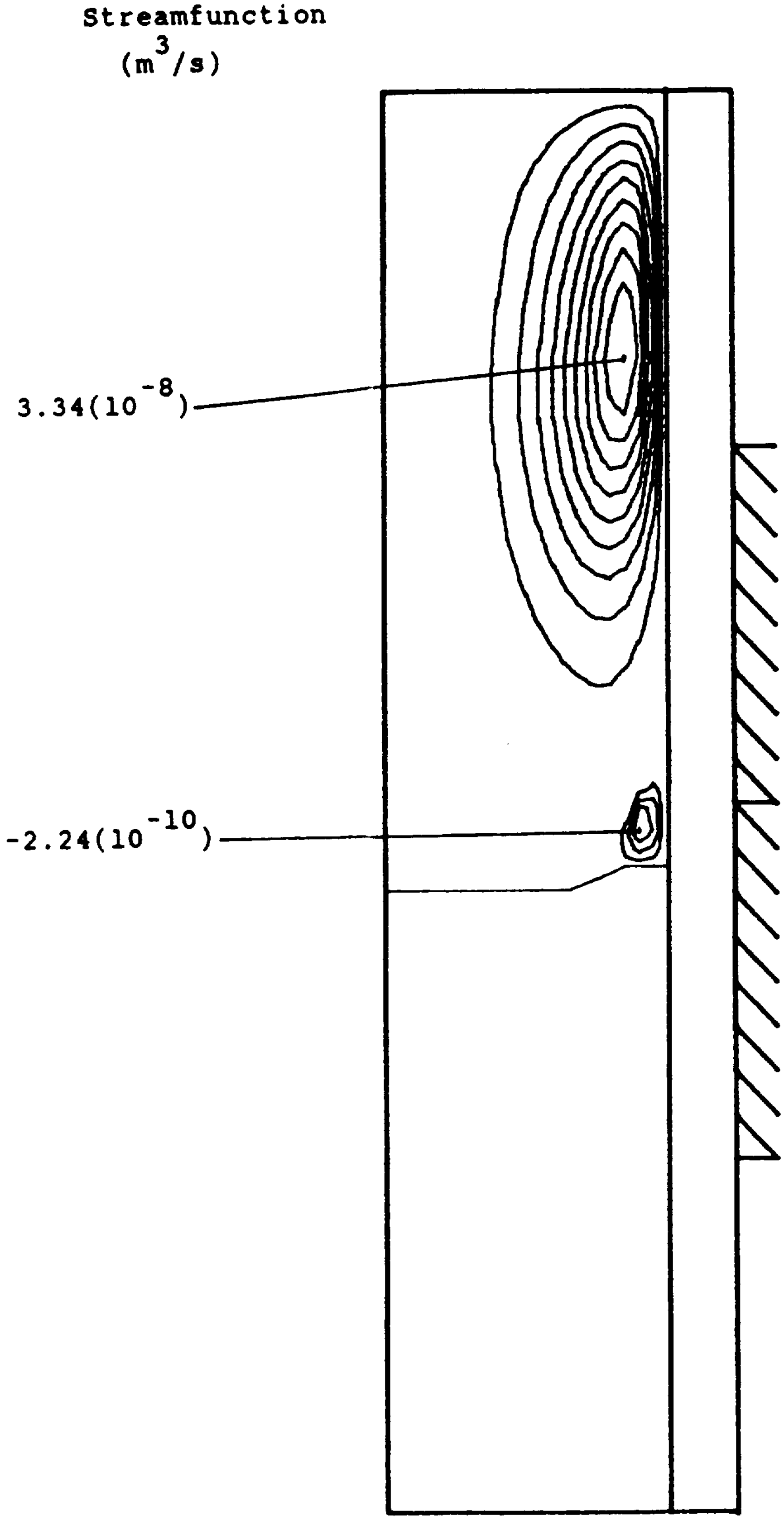

Figure 5.3 Thermal convection streamlines. $V_{max} = 6.0(10^{-3})$ m/s, Gravitational field strength = $9.8\ (10^{-2})\ m/s^2$.

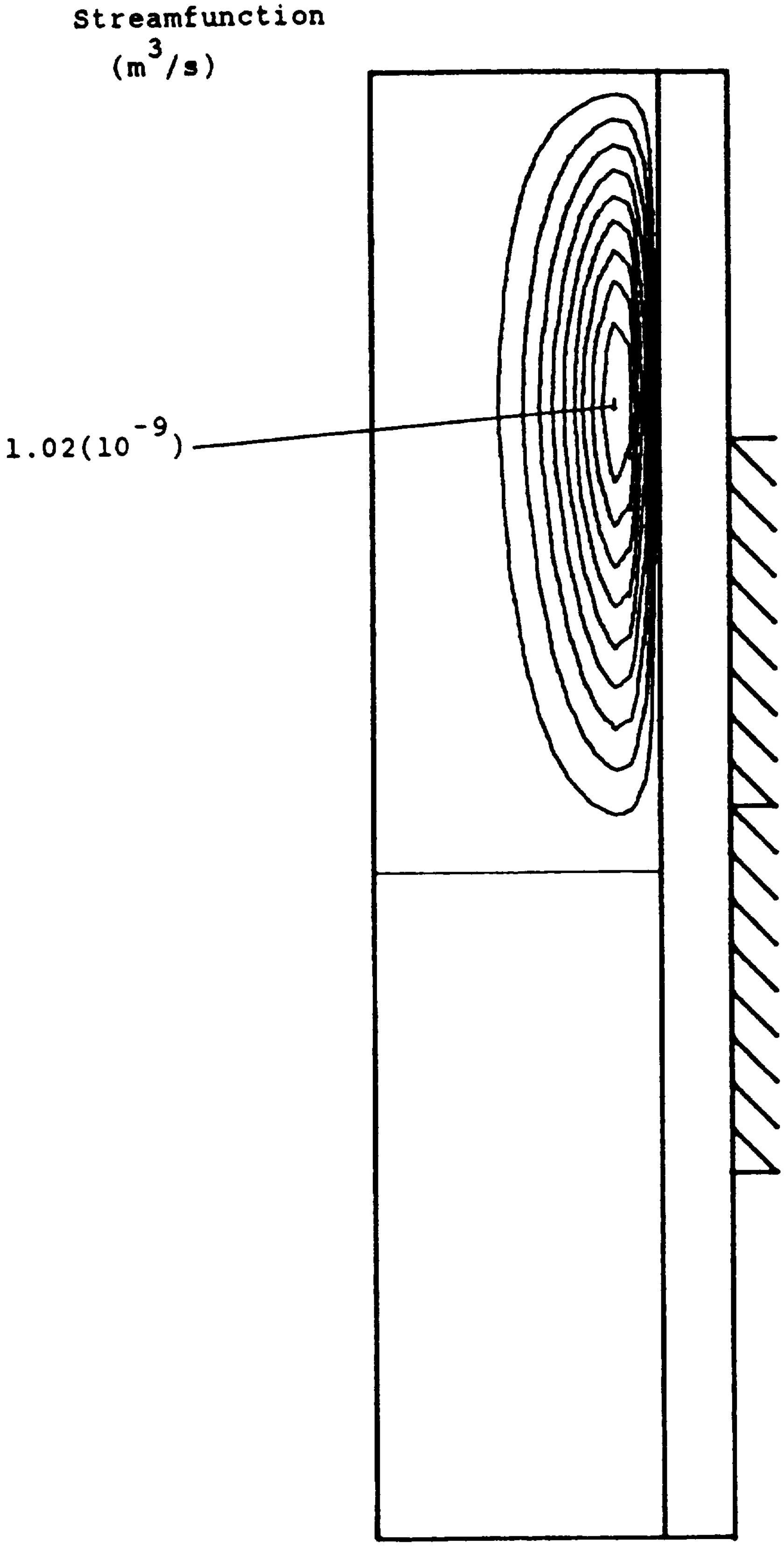

Figure 5.4 Thermal convection streamlines. $V_{max} = 2.0(10^{-4})$ m/s, Gravitational field strength = 9.8 (10^{-4}) m/s^2.

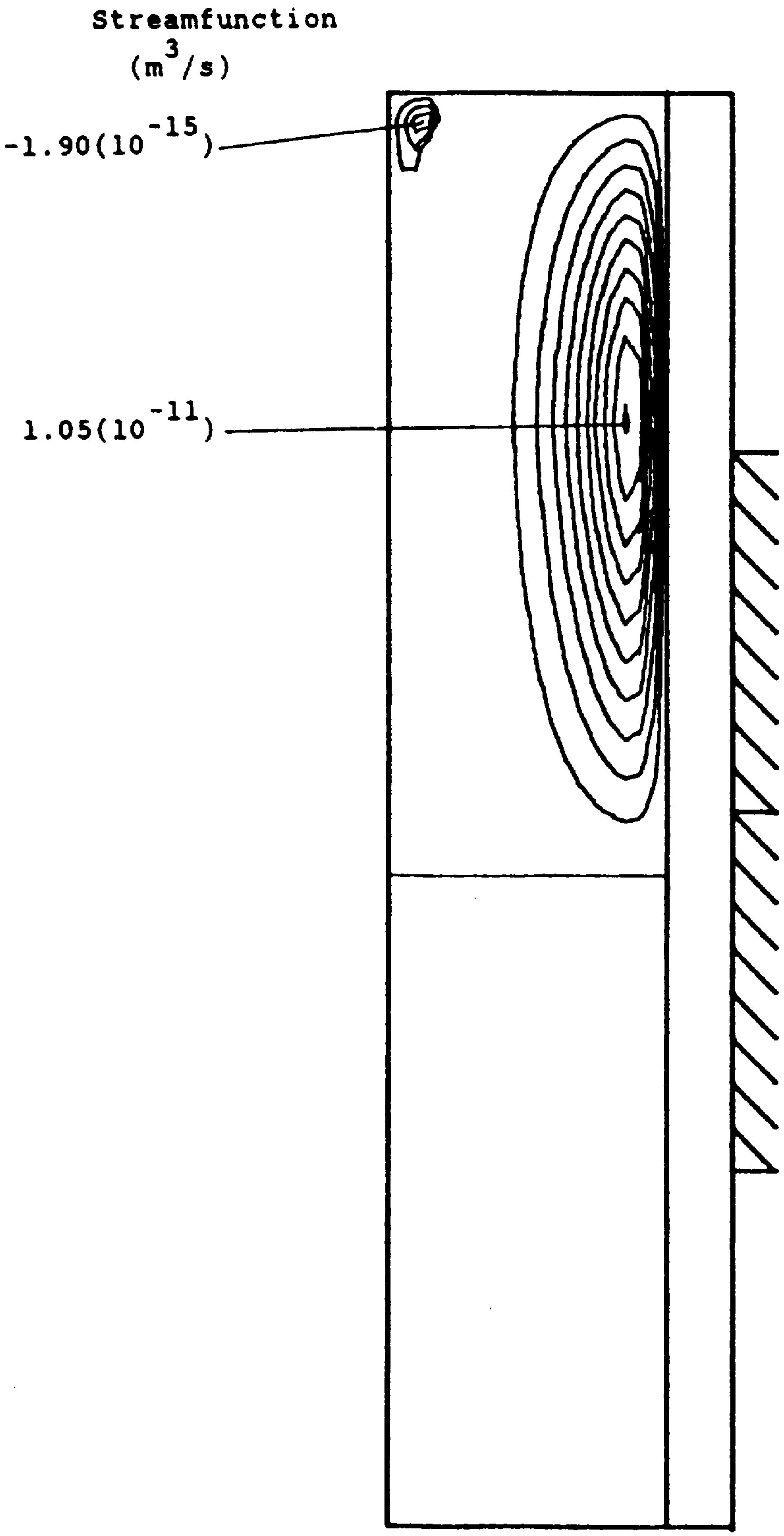

Figure 5.5 Thermal convection streamlines. $V_{max} = 2.1(10^{-6})$ m/s, Gravitational field strength = $9.8\ (10^{-6})$ m/s^2.

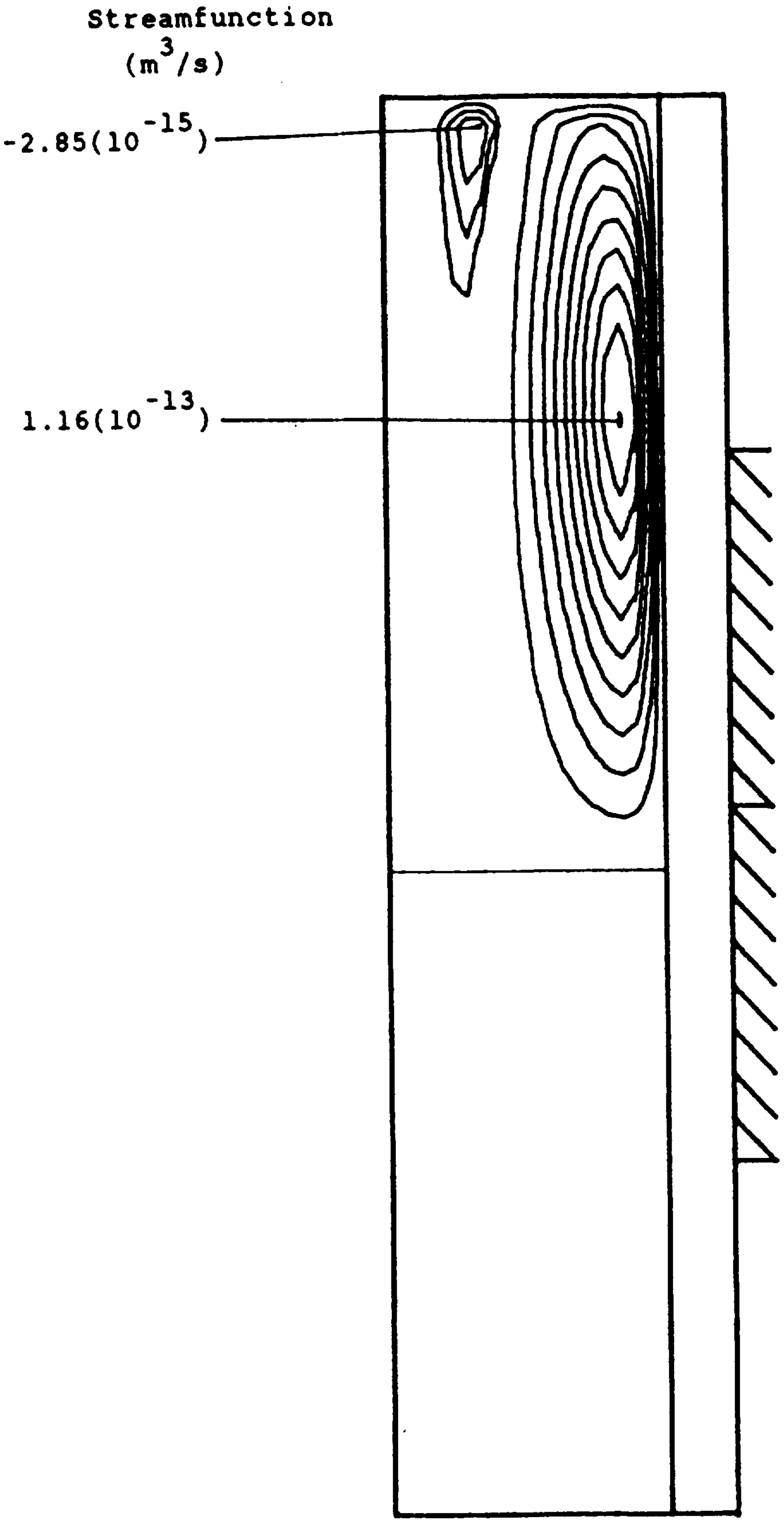

Figure 5.6 Thermal convection streamlines. $V_{max} = 2.9(10^{-8})$ m/s, Gravitational field strength = $9.8\ (10^{-8})\ m/s^2$.

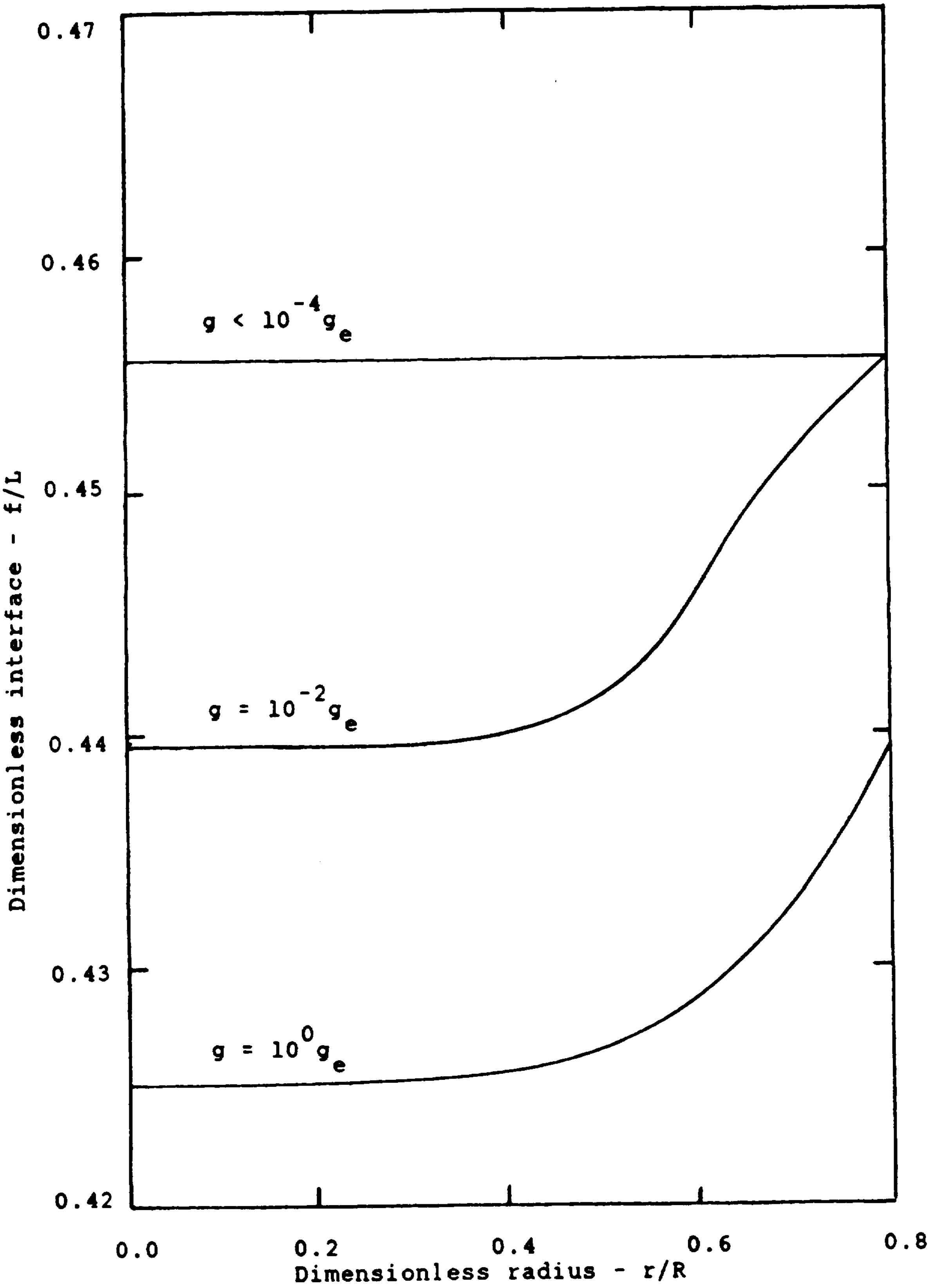

Figure 5.7 Melt solid liquid interface shape for various gravitational field strengths.

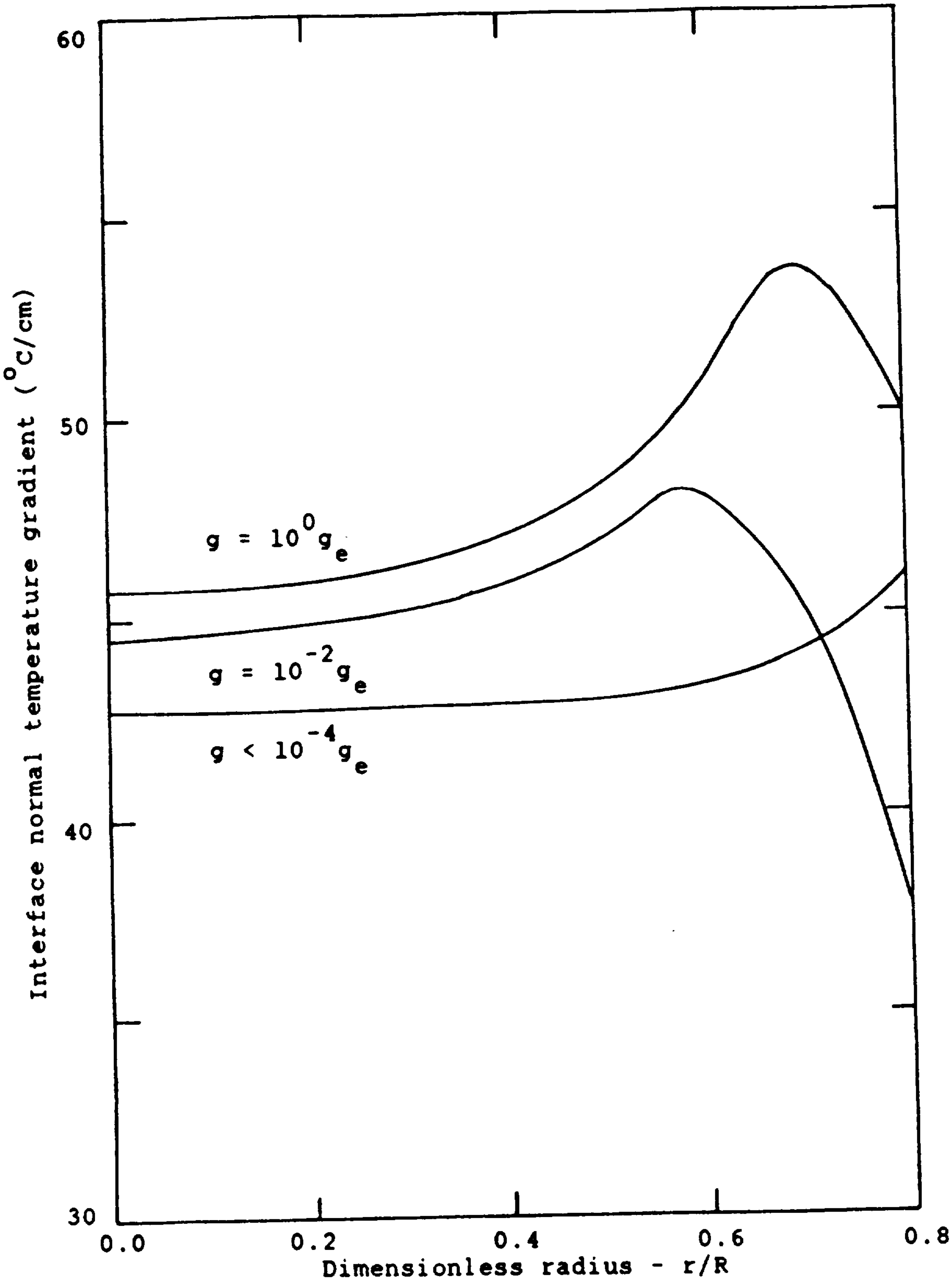

Figure 5.8 Interface normal temperature gradient for various gravitational field strengths.

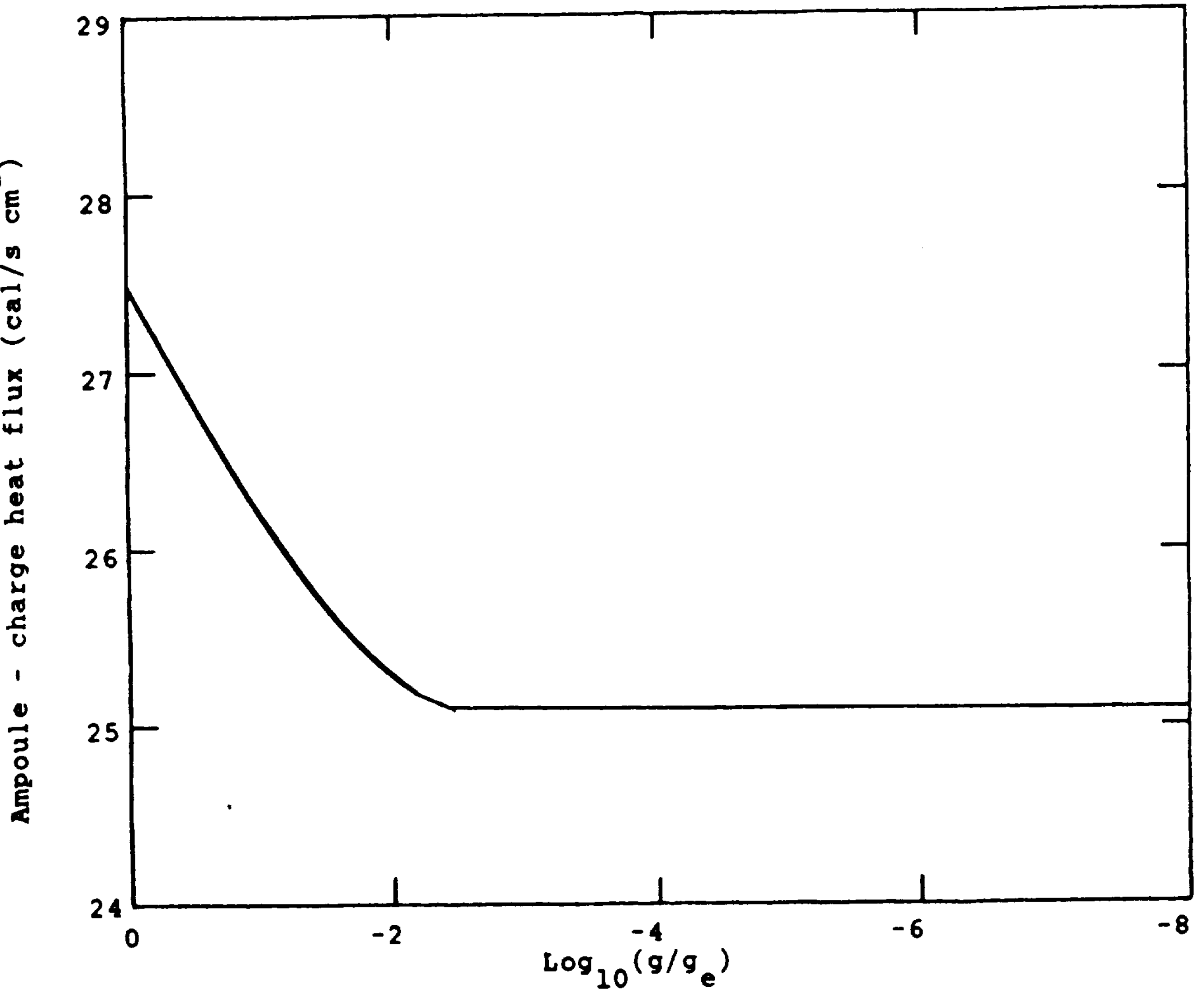

Figure 5.9 Total heat transfer for various gravitational field strengths.

6.0 Effect of Coriolis Acceleration

A preliminary study was conducted to determine how orbital rotation would influence the melt flow field. This in turn would alter the advective transport processes if changes in flow velocity were significant. A three dimensional simulation was processed for the configuration of Section 5, where only thermal convection was considered. The flow velocity resulting from axisymmetric thermal convection is believed to be representative of conditions in the absence of orbital motion. Figure 6.1 shows the ampoule during various stages of an orbit around the Earth. An angular rotation of one revolution per day is superimposed on the axisymmetric flow of Section 5. The axisymmetric flow is the same as in Figure 5.4 where the gravitational field strength is $9.8(10^{-4})$ m/s^2. The axis of the ampoule is always aligned with a radial line from the center of rotation to the ampoule axis origin.

The results are presented in Figures 6.2 - 6.5. An asymmetry in the azimuthal velocity is seen if Figures 5.2 and 5.3 where maximum angular velocities are of the order of 10^{-5} cm/s. These are small when compared to axial velocities (Figures 6.4 and 6.5). A six fold increase in maximum velocity is realized when orbital rotation is taken into account as shown below.

Orbital Velocity rev/day	Maximum Velocity cm/s	Azimuthal velocity cm/s
0	$2.0(10^{-2})$	0
1	$13.1(10^{-2})$	$5.4(10^{-5})$

These velocities are still very small. Whether or not the difference is significant will be determined in future studies, but the current results indicate that such a study would be worthwhile.

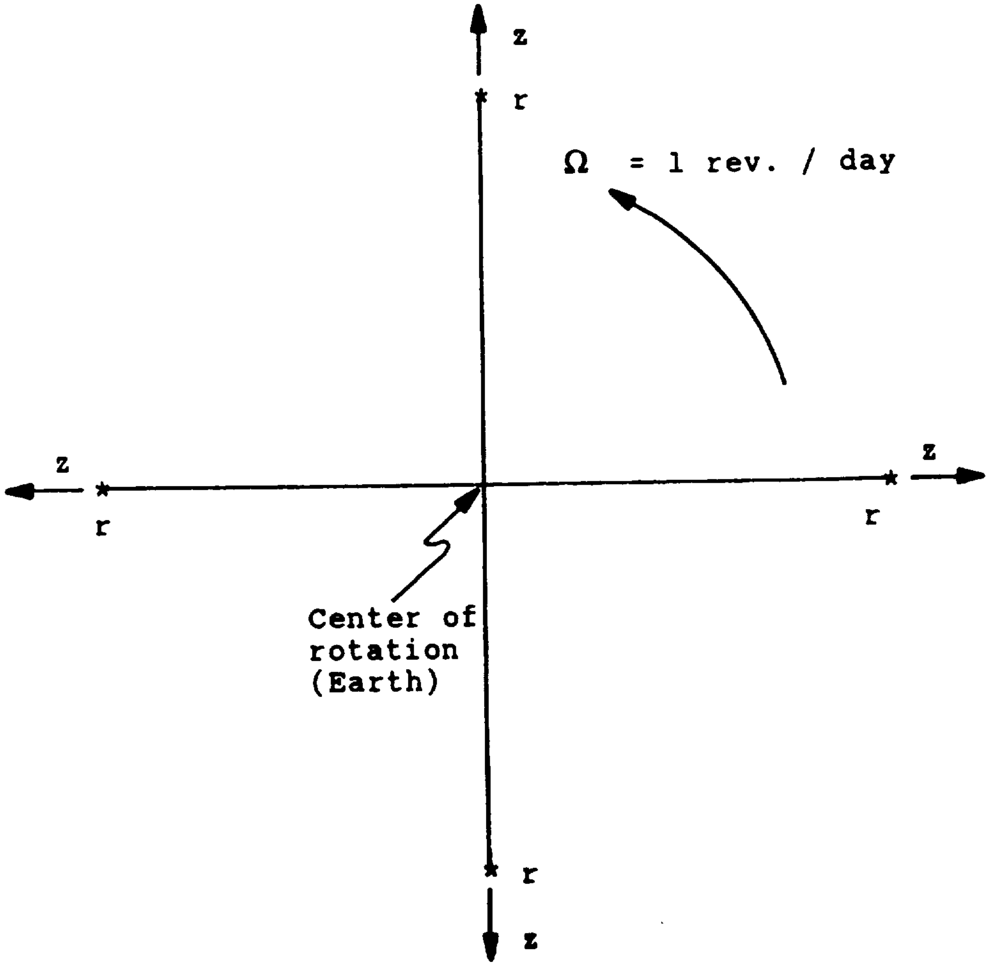

Note: 1. Azimuthal coordinate measured clockwise from normal to plane of motion.

2. * = origin of ampoule.

Figure 6.1 Ampoule orbit alignment in plane of motion.

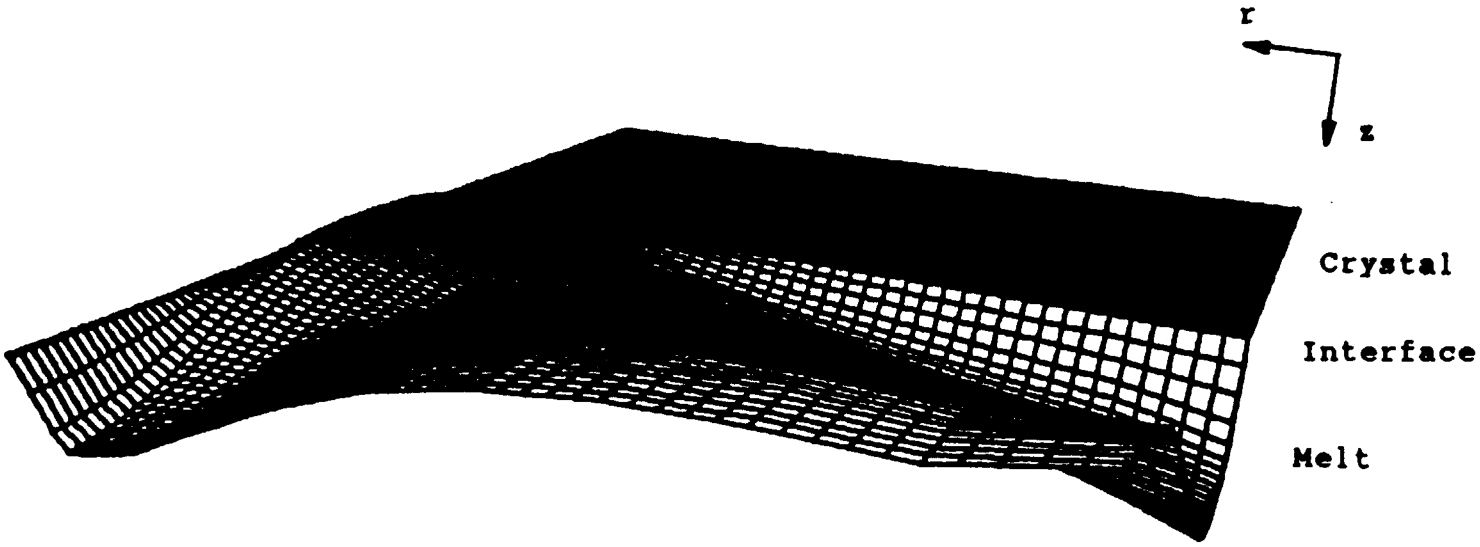

$V_{\theta\ max} = +5.4(10^{-5})$ cm/s.

$V_{\theta\ min} = -4.1(10^{-5})$ cm/s.

Figure 6.2 Azimuthal velocity at $\theta = 0^{\circ}$.

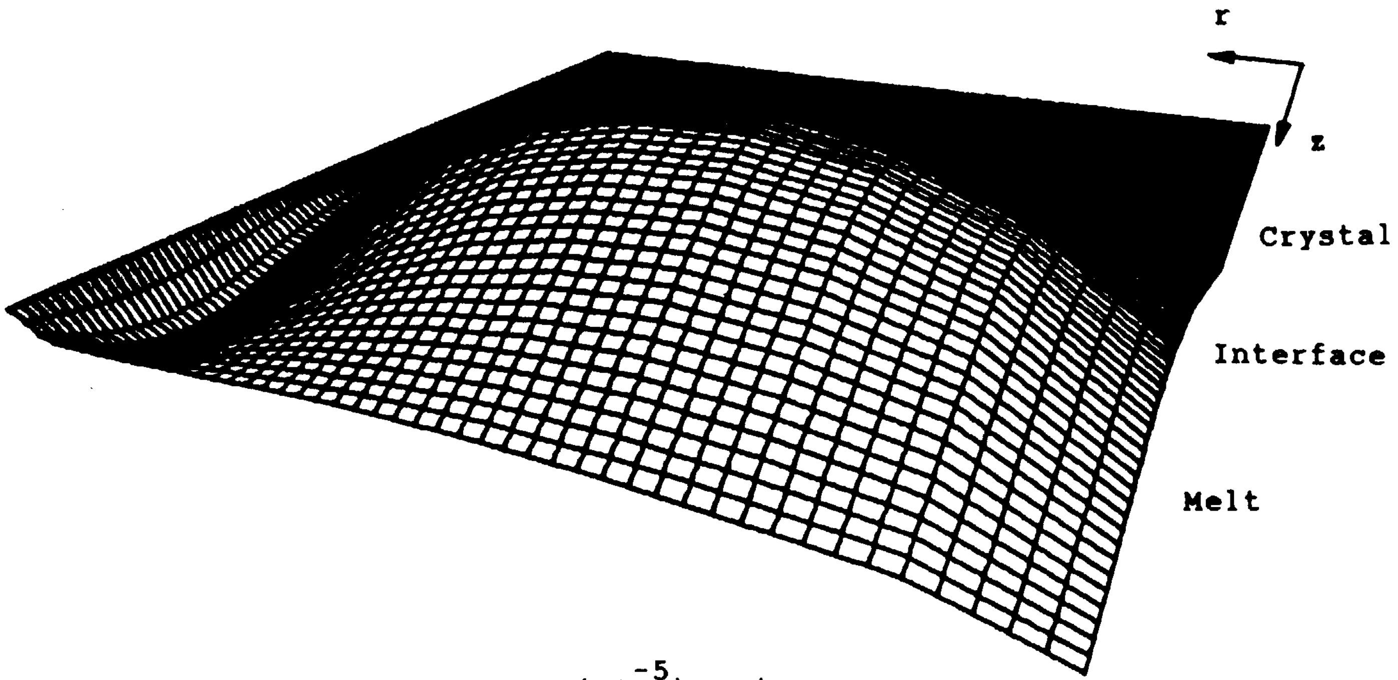

$V_{\theta\ max} = +1.5(10^{-5})$ cm/s.

$V_{\theta\ min} = -5.3(10^{-6})$ cm/s.

Figure 6.3 Azimuthal velocity at $\theta = 180^{\circ}$.

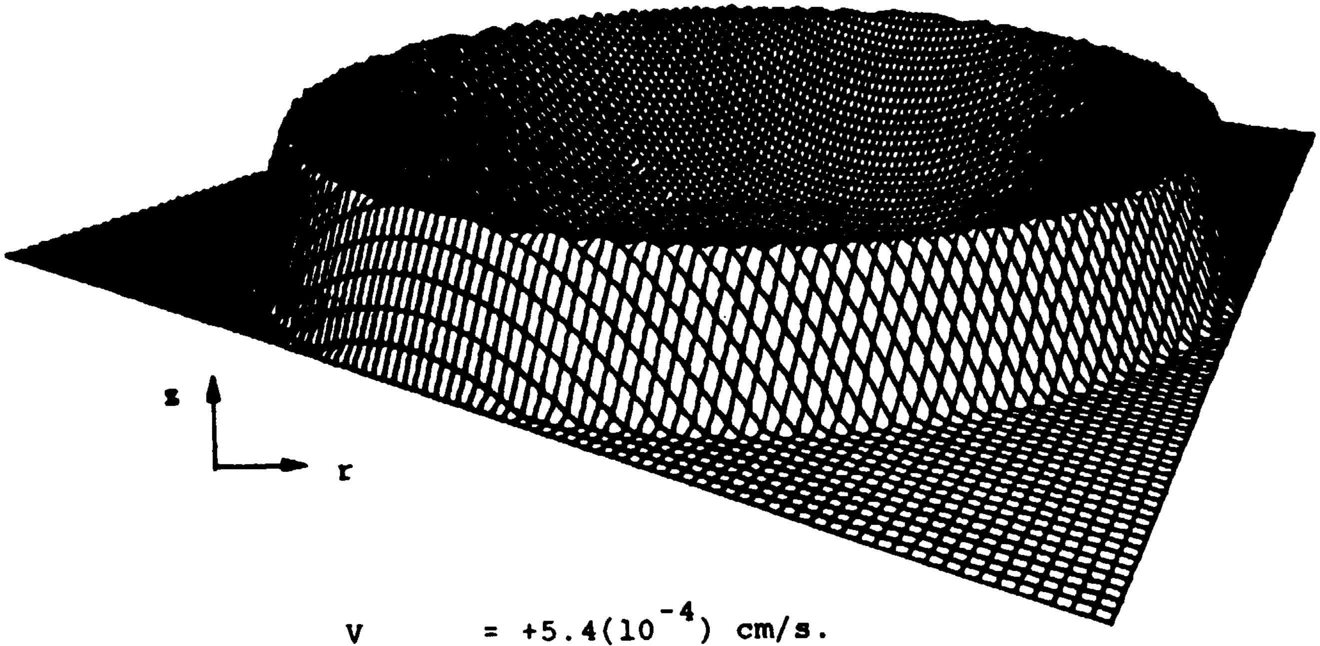

$V_{z\ max} = +5.4(10^{-4})$ cm/s.

$V_{z\ min} = -6.9(10^{-4})$ cm/s.

Figure 6.4 Axial velocity at z/L = 0.464 into the melt. Interface at z/L = 0.456.

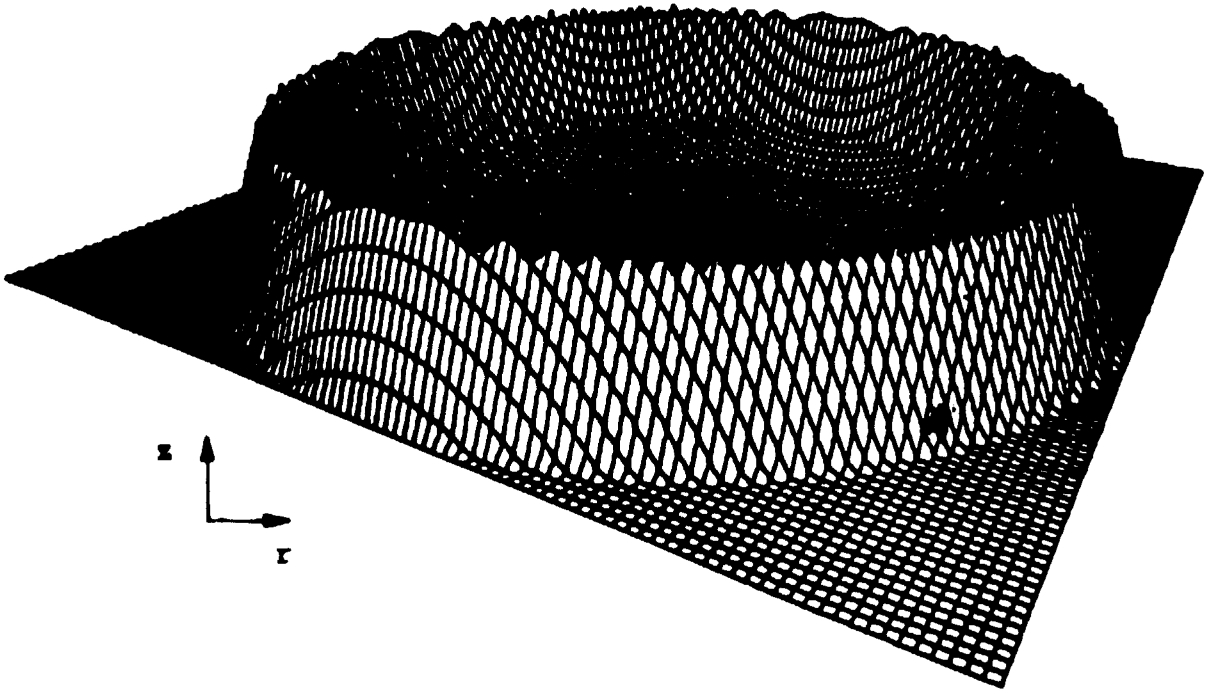

$V_{z\ max} = +5.5(10^{-2})$ cm/s.

$V_{z\ min} = -4.7(10^{-2})$ cm/s.

Figure 6.5 Axial velocity at z/L = 0.687 into the melt. Interface at z/L = 0.456.

7.0 Thermosolutal Convection

Melt growth of binary and pseudo-binary alloys with large liquidus - solidus separation is complicated by the interactions between the concentration distribution in the melt and heat transfer in both the melt and crystal. The composition of the melt, and the solidification temperature are linked by the phase diagram for the alloy. The melt flow field caused by the buoyancy effect due to the axial gravitational field and the radial density gradient. The radial density gradient is a function of the temperature and concentration distribution in the melt. The melt flow field can have a substantial influence on the species transport process of semiconductors which are characterized by high Schmidt numbers. Since these fields are interactive with each other, any assumptions or simplifications in the model on the fields may introduce inaccuracies into the results. The purpose of the following study is to evaluate the effect of temperature and concentration variations in the melt on the flow field and on the crystal growth rate, interface shape, and solute concentration distribution.

The thermophysical properties for this study are those of PbSnTe. This is thermally stable and solutally unstable (in a one dimensional sense) for the vertical growth configuration. Geometrically the growth system consists of a three zone furnace shown in Figure 5.1. Two thermally stable cases were investigated: Case A, solutally unstable, and Case B, solutally stable. Both use the same equilibrium phase diagram (Figure 7.1) and thermophysical properties except that the sign of the solutal coefficient of volume expansion (+1.2/Wt.% for stable flow) is reversed.

Initially the ampoule is centered in the adiabatic zone and is in a steady state thermal convection mode and not translating. The flow is driven by a $9.8(10^{-4})$ m/s^2 axial gravitational field and the interface temperature is 937°C. This corresponds to zero concentration in the melt. At time equal to zero the ampoule pull rate is increased to 5 cm/hr and a uniform melt mass fraction of 0.2 is impressed on the system.

Case A will be described first and then the differences between the cases will be highlighted. The interface position as the solidification progresses through the ampoule is shown in Figure 7.2. No movement is seen in the first 200 s as the interface temperature adjusts to its new lower equilibrium value. The crystal was not allowed to remelt. A more realistic situation would have been a melt back followed by a resolidification. Between 200 s and 700 s is a transient growth phase where the interface growth rate, V_f, and ampoule withdrawal velocity, V_p, are not the same. The initially planar interface now becomes concave and the curvature continues to change with time. This is followed by a steady state phase between 700 s and 1370 s in which these two rates are equal. Bulk concentration continually changes during all phases of the process. Finally, the side of the ampoule is lowered to a position within the adiabatic zone, and since the top is insulated, rapid solidification ensues until the entire charge is crystalized at 1810 s.

Figure 7.3 shows the concentration field throughout the charge at 506 s. Notice that the interface is not at a constant axial position but varies with the radius. In this plot it lies between $z = 4.05$ and 4.15. Inspection will reveal that it is concave. The liquid region immediately in front of the interface is a thin layer (approximately 0.5 cm) of rapidly decreasing concentration. This is the concentration boundary layer. There is also a radial gradient in the liquid (say at $z = 5.5$) outside this layer due to a single advection cell in the bulk. This contrasts with the dual celled solutally stable Case B which has a correspondingly smaller gradient.

A 1810 s the charge is completely solidified. The concentration distribution in the solid will now be described with the help of Figure 7.2 and Figure 7.4.

$3.5 < z < 3.75$, $(0 < t < 450 \text{ s})$

This is the initial transient period with the interface adjusting to the step change in bulk concentration. The interface temperature must drop from 937°C to 918°C. V_f is zero until about 200 s has passed. Then V_f increases from zero to some value greater than V_p and C_s increases.

$3.75 < z < 4.0$, $(450 < t < 700 \text{ s})$

Interface velocity decreases and then increases. Simultaneous with this C_s increases and then decreases. This always happens and other researchers have noticed it[e.g.,13,14].

$4.0 < z < 4.9$, $(700 < t < 1400 \text{ s})$

Steady state growth with continuously changing bulk concentration. $V_f = V_p = 5$ cm/hr = slope of the curve in Figure 7.2. This is a region of large radial segregation.

$4.9 < z < 7.5$, $(1400 < t < 1800$ s)

The side of the ampoule is now entirely within the adiabatic zone. No energy enters the charge since the top of the ampoule is insulated. V_f exceeds V_p as shown. This increase in interface velocity dictates an increase in C as previously mentioned, but the overall species conservation demands a general decrease. The characteristic increase in C in the vicinity of the "last to freeze" is not quite as dramatic as it should be because of the rather large computational volumes and the averaging technique used.

Two curves corresponding to those just presented are given in Figures 7.6 and 7.6 for solutally stable Case B. Differences between the two cases will now be discussed with the aid of Table 7.1. Case A is primarily single celled advection with a second, much weaker cell appearing for short time intervals but always fading. The melt velocity increases from the initial thermally driven flow to 3.62 cm/s and then decreases. The interface is essentially planar from the ampoule centerline to about $r/R = 0.5$ after which it becomes concave.

In Case B, two counterrotating cells are present for most of the process except at the very beginning and at the end. The melt velocity is maximum at $2.0(10^{-2})$ cm/s at time equal to zero and then steadly decreases to zero. The upper cell is always stronger than the lower cell but is extinguished at the end of the process before the lower cell. The magnitude of the maximum velocity is always less than that of Case A at corresponding times. The concave interface is usually planar between r/R = 0.0 and 0.7.

Initial Condition: C = 0, Thermal convection

Maximum Streamfunction = $1.1(10^{-3})cm^3/s$, $V_{max} = 2(10^{-2})cm/s$

Solutally Stable - Case A

t	Maximum Streamfunction		V_{max}
s	Primary Cell	Secondary Cell	cm/s
0	$1.00(10^{-3})$	-	$2.00(10^{-2})$
280	$1.00(10^{-3})$	-	$1.96(10^{-2})$
506	$1.74(10^{-3})$	-	$3.60(10^{-2})$
748	$1.62(10^{-3})$	$-6.90(10^{-8})$	$3.30(10^{-2})$
1078	$1.70(10^{-3})$	-	$3.60(10^{-2})$
1392	$6.10(10^{-4})$	$-2.00(10^{-6})$	$1.20(10^{-2})$
1441	$7.40(10^{-5})$	-	$1.20(10^{-3})$

Solutally Unstable - Case B

t	Maximum Streamfunction		V_{max}
s	Primary Cell	Secondary Cell	cm/s
0	$1.00(10^{-3})$	-	$2.00(10^{-2})$
288	$9.20(10^{-4})$	$-3.50(10^{-6})$	$1.80(10^{-2})$
505	$7.50(10^{-4})$	$-1.90(10^{-6})$	$1.50(10^{-2})$
747	$5.40(10^{-4})$	$-6.80(10^{-6})$	$1.10(10^{-2})$
1085	$3.60(10^{-4})$	$-6.50(10^{-6})$	$7.10(10^{-3})$
1400	$7.50(10^{-6})$	$-8.40(10^{-6})$	$1.60(10^{-4})$
1448	-	$-2.70(10^{-7})$	$6.00(10^{-6})$

Table 7.1 Primary and secondary cell streamfunction (cm^3/s) and maximum velocity (cm/s) versus time for (a), Case A Unstable and (b), Case B Stable convection.

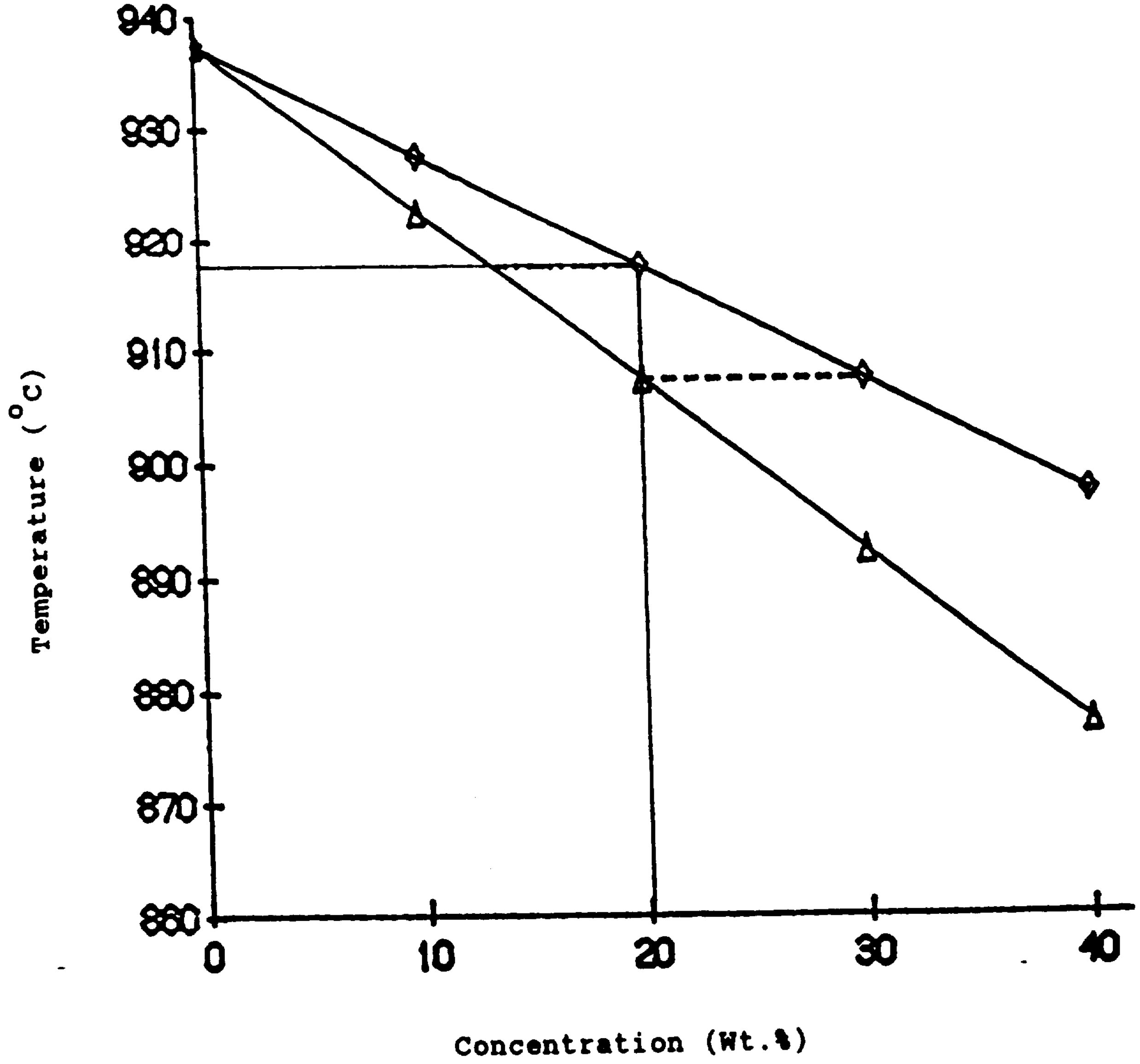

Figure 7.1 Phase diagram for $Pb_{1-x}Sn_xTe$. Segregation coefficient = 2/3.

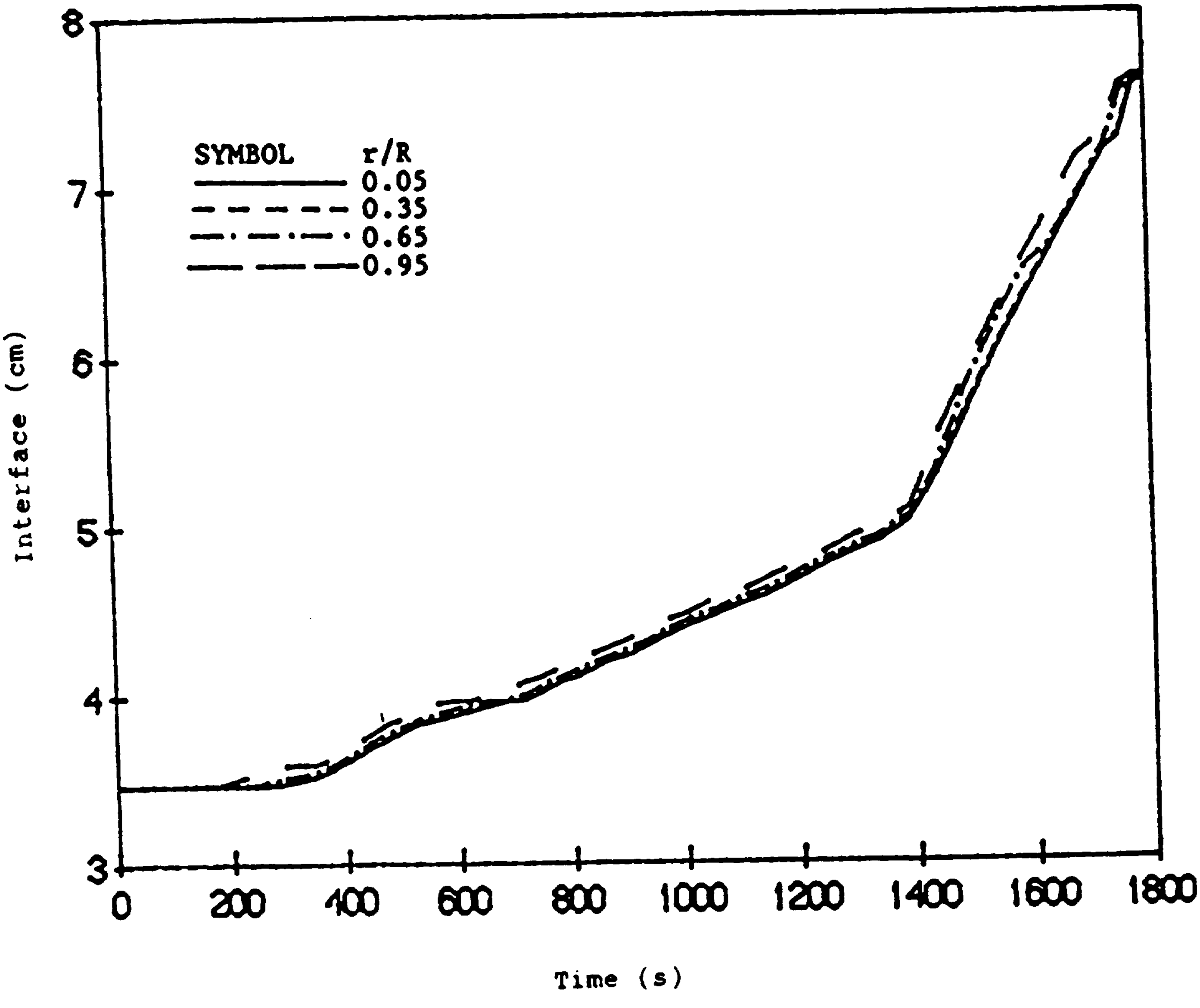

Figure 7.2 Interface position versus time for thermally stable, solutally unstable convection.

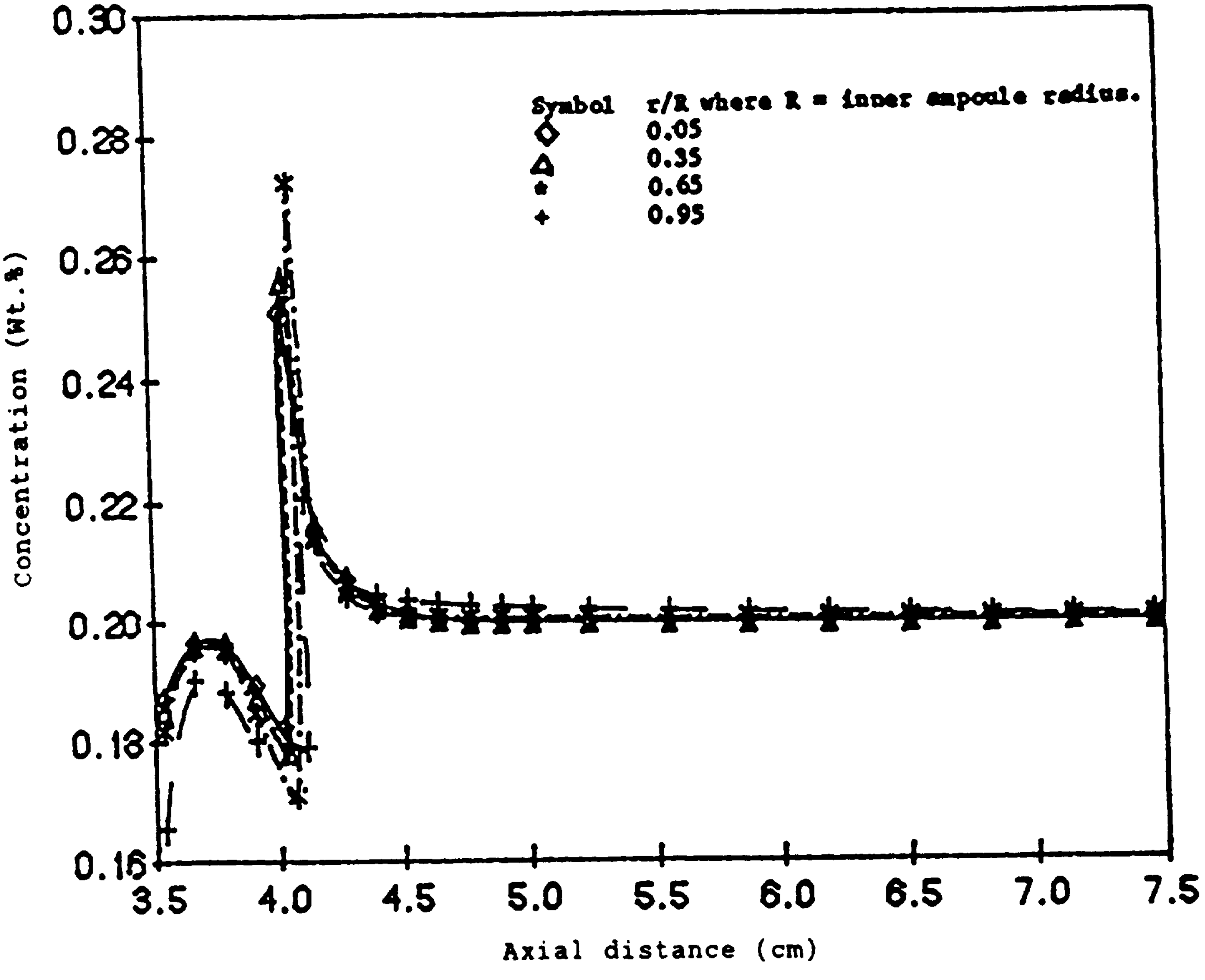

Figure 7.3 Charge concentration field when partially solidified at 506 s for thermally stable, solutally unstable convection.

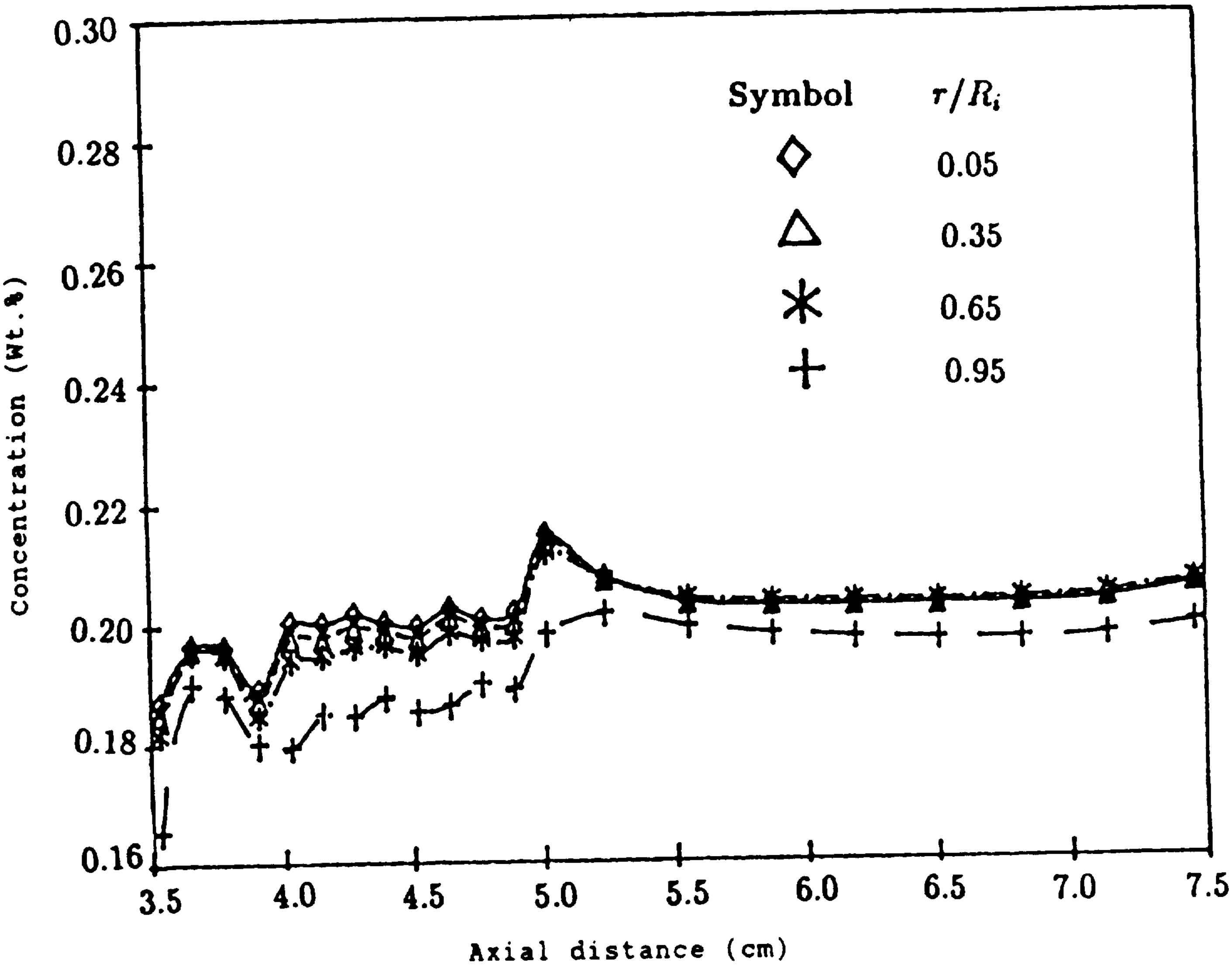

Figure 7.4 Charge concentration field when completely solidified at 1810 s for thermally stable, solutally unstable convection.

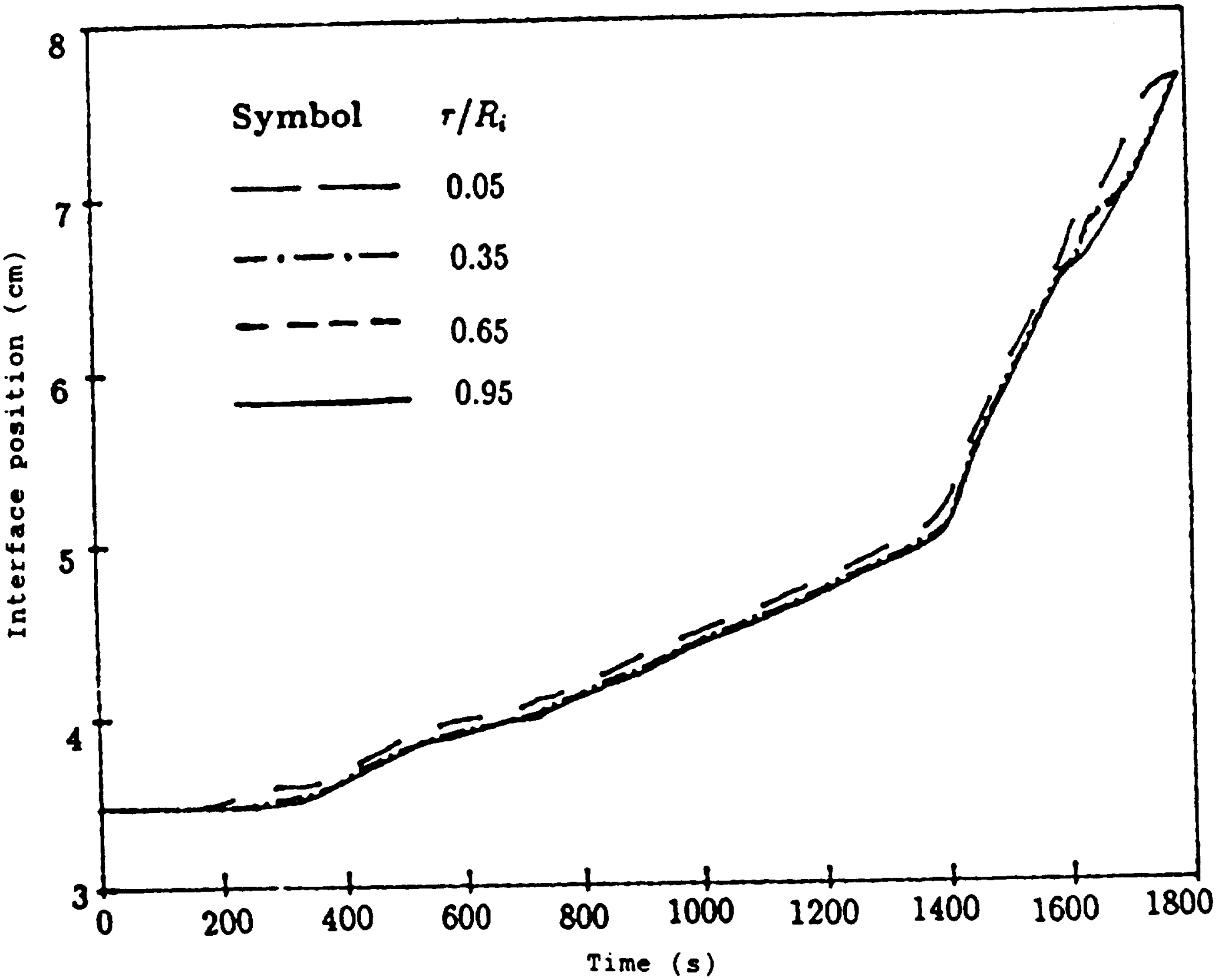

Figure 7.5 Interface position versus time for thermally stable, solutally stable convection.

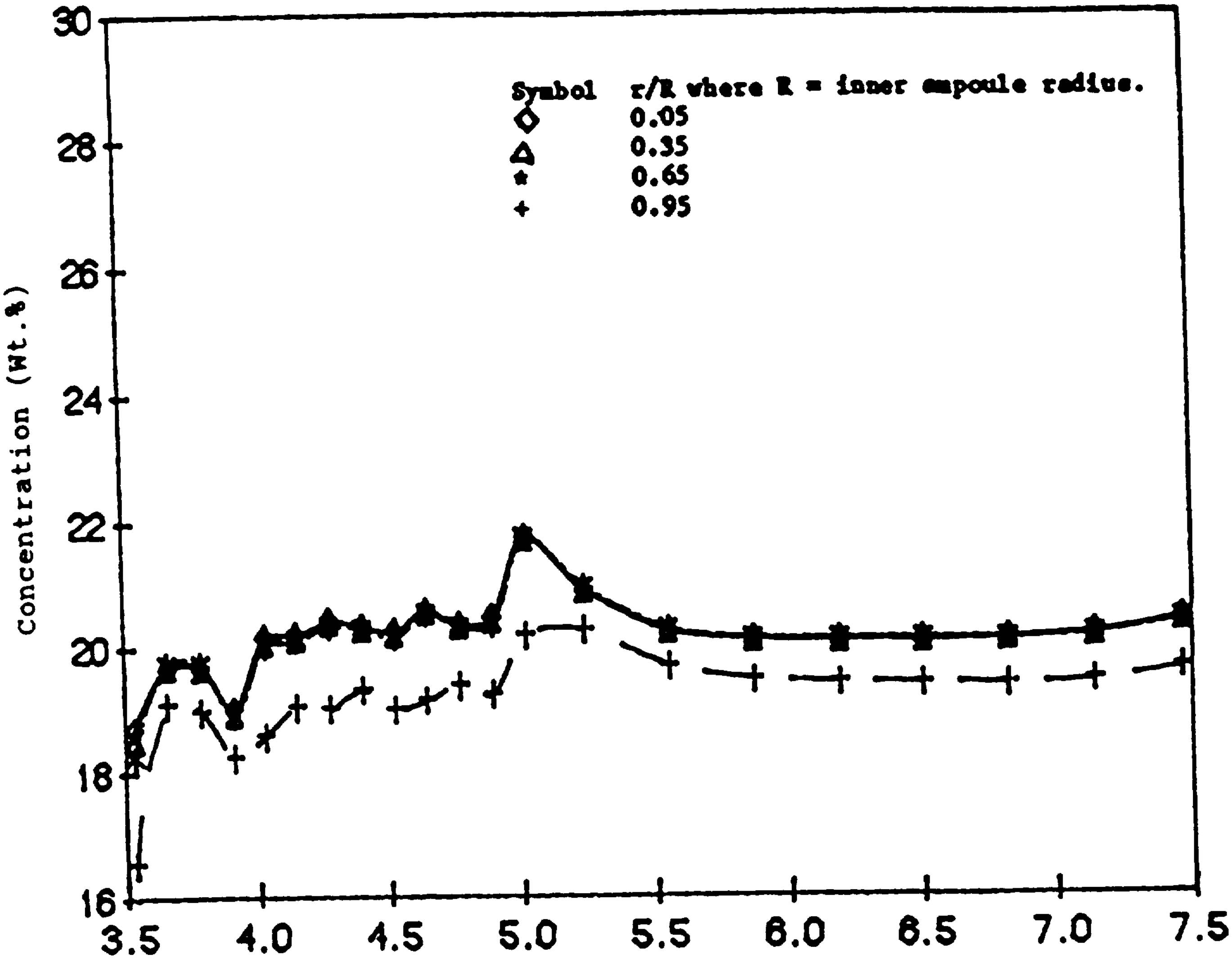

Figure 7.6 Charge concentration field when completely solidified at 1800 s for thermally stable, solutally stable convection.

Nomenclature

A	Area (m^2)
a	Charge radius (m)
a_l, a_s, a_w	Liquid, solid, wall thermal diffusivity (m^2/s)
C	Species mass fraction
Cp	Specific heat (J/g K)
D	Species diffusivity (m^2/s)
f	Interface (m)
g	Local axial gravitiational field (m/s^2)
g_e	Earth gravitational field strength - 9.80 m/s^2
G	Dimensionless gravity, g/g_e
H	Latent heat, (cal/g)
K	Thermal conductivity (W/m K)
k	Segregation coefficient, $=C_s/C_l$ on f
L	Length of ampoule, (m)
n	Normal to surface (m)
N	Curvature index - $(z_o-z_w)/a$
p	Pressure (N/m^2)
Pr	Prandtl number
q	Heat flux - Fourier's Law (W/m^2)
Q	Heat transfer from hot zone to cold zone ($cal/s\ cm^2$)
r	Radial coordinate (m)
R	Ampoule outside radius (m)
Sc	Schmidt number
t	Time (s)
T	Temperature (K)
u	Radial velocity (m/s)

v	Axial velocity (m/s)
V	Vector velocity (u,v), (m/s)
V_f	Interface velocity (m/s)
V_p, V_{pull}	Ampoule withdrawal velocity (m/s)
z	Axial coordinate (m)
z_0	Axial coordinate at $r = 0$ (m)

Greek symbols

β_t	Thermal coefficient of volume expansion, (C^{-1})
β_s	Solutal coefficient of volume expansion, (/Wt.%)
Γ	Dimensionless density
δ	Thermophysical property in conservation equation
θ	Cylindrical coordinate (degree)
μ	Molecular viscosity (N s/m^2)
ν	Kinematic viscosity (m^2/s)
ρ	Density (kg/m^3)
σ	Dependent variable in conservation equation
ϕ	Dependent variable in conservation equation
ψ	Streamfunction (cm^3/s)
Ω	Orbital angular velocity (/s)

Subscripts

c	cool zone of furnace wall
f	interface
h	hot zone of furnace wall
l	liquid (melt)
s	solid (crystal)
w	wall (ampoule)

References

1. R.B. Bird, W.E. Stewart, E.N. Lightfoot, Transport Phenomena, John Wiley, New York (1960).

2. Hirt, C.W., Nichols, B.D., and Romero, N.C. "SOLA - A Numerical Solution Algorithm for Transient Fluid Flow," Report No. LA-5852, Los Alamos Scientific Laboratory, Los Alamos, New Mexico, April 1975.

3. R.A. Gentry, R.E. Martin, B.J. Daly, An Eulerian Differencing Method for Unsteady Compressible Flow Problem. J. Comput. Phys. 1 (1966) 87-118.

4. F.H. Harlow, A.A. Amsden, Fluid Dynamics: An Introductory Text, LA-4281, Los Alamos National Laboratory, Los Alamos, NM., (1969)

5. P.J. Roache, Computational Fluid Dynamics, Hermosa Publishers, Albuquerque, NM. (1976)

6. A.H. Eraslan, W.L. Lin, R.D. Sharp, "FLOWER: A Computer Code for Simulating Three-Dimensional Flow, Temperature and Salinity Conditions in Rivers, Estuaries and Coastal Regions". ORNL/NUREG-8401, Oak Ridge National Laboratory, Oak Ridge, Tennessee, December 1983.

7. L.Y. Chin, F.M. Carlson, Finite Element Analysis of the Control of Interface Shape in Bridgman Crystal Growth. J Crystal Growth 62 (1983) 561-567.

8. S.R. Coriell, R.F. Sekerka, Lateral Solute Segregation During Unidirectional Solidification of a Binary Alloy With a Curved Solid-Liquid Interface. J. Crystal Growth, 46, 479-482.

9. S.R. Coriell, R.F. Boisvert, R.G. Rehm, R.F. Sekerka, Lateral Solute Segregation During Unidirectional Solidification of a Binary Alloy with a Curved Solid-Liquid Interface, II. Large departures from planarity. J Crystal Growth 54 (1981) 167-175.

10. P.C. Sukanek, Deviation of Freezing Rate From Translation Rate in the Bridgman-Stockbarger Technique. J. Crystal Growth, 58 (1982) 208-228.

11. S.L. Lehoczky, F.R. Szofran, Directional Solidification and Characterization of HgCdTe Alloy. Materials Processing in the Reduced Gravity Environment of Space, G.E. Rindone (Ed.), vol 9, North Holland 409-420.

12. D. Camel, J.J. Favier, Thermal Convection and Longitudinal Macrosegregation in Horizontal Bridgman Crystal Growth. J. Crystal Growth, 67 (1984) 42-56.

13. Smith, Tiller, Rutter, Canadian Journal of Physics, 33 (1955) 723-745.

14. E. Bourret, R. Derby, R. Brown, J Crystal Growth 71 (1985) 587-596.